Journal of Computational Applied Mechanics 2027, 58(1): 140-175

DOI: 10.22059/jcamech.2026.426891.2025

RESEARCH PAPER

Analysis of Love waves in double-porosity layered medium under Moore-Gibson-Thompson theory of thermo-elasticity

Anand Kumar Yadav [a, *], Pranali Kamdi [b], Vinod Varghese [c], Marin Marin [d, e, †]

[a] *Department of Applied Science, Advanced Centre of Research and Innovation, School of Engineering and Technology, CGC Unjversity, Mohali, Punjab-140307, India*

[b] *Department of Mathematics, School of Science, G. H. Raisoni University Saikheda, Sausar, Madhya Pradesh, India*

[c] *Department of Mathematics, M.G. College, Armori, Gadchiroli, India*

[d] *Faculty of Mathematics and Computer Science, Transilvania University of Brasov, Brasov, Romania*

[e] *Academy of Romanian Scientists, Ilfov Street, No. 3, 050045 Bucharest, Romania*

Abstract

This study presents a generalized model for Love-type surface wave propagation in layered thermoelastic media with double porosity, incorporating Moore–Gibson–Thompson (MGT) theory to capture causal and dissipative thermal effects. The configuration consists of a finite elastic layer perfectly bonded to a semi-infinite half-space, with each domain exhibiting distinct porosity and thermal properties. Using the normal mode method, the governing equations are formulated and solved to derive dispersion relations for coupled wave fronts. The analysis reveals two distinct wave fronts: the first replicates classical Love wave behavior, independent of thermal and porosity effects. In contrast, the second emerges from the interplay between thermal relaxation and dual porosity structures. Unlike previous Green–Naghdi type III (GN-III) models, the second front under MGT theory is attenuating, frequency-sensitive, and vanishes in the low-frequency limit. Numerical simulations demonstrate the influence of void parameters and thermal conductivity on phase velocity, attenuation, and energy flux. These findings are directly relevant to engineering practice. For example, frequency-dependent attenuation curves can guide the design of ultrasonic sensors for nondestructive testing, while dispersion relations inform seismic inversion techniques for subsurface characterization. The energy partitioning analysis also provides insight into microscale material diagnostics, where thermo-poroelastic coupling affects reliability in composite structures. Thus, the study extends the theoretical foundation while offering concrete pathways for application in seismic exploration, ultrasonic sensing, and microscale material engineering.

Keywords: Love waves; double porosity; thermoelasticity; MGT theory; dispersion relation; wave attenuation

1. Introduction

The propagation of surface waves in layered elastic media has long been a subject of profound interest in

* Corresponding author: Anand Kumar Yadav. *E-mail address* yadavanand977@gmail.com

† Corresponding author: Marin Marin. *E-mail address*: m.marin@unitbv.ro

geophysics, seismology, and applied mechanics. Among these, Love-type waves characterized by horizontally polarized shear motion play a pivotal role in interpreting seismic data and assessing subsurface structures. The foundational work by Ewing et al. [1] established the basis for dispersion analysis in stratified media, and subsequent studies have extended this framework to increasingly complex configurations.

Classical Love Waves

Classical models assume an isotropic elastic layer overlying a homogeneous half-space, where wave energy remains trapped within the layer, leading to frequency-dependent dispersion. This behavior has been extensively studied in anisotropic [2], poroelastic [3], viscoelastic [4], and corrugated geometries [5]. Further extensions include reinforced [6], inhomogeneous [7], and periodic boundary structures [8], highlighting the sensitivity of Love waves to material gradation and geometry.

Poroelastic and Double-Porosity Frameworks

The theory of elastic materials with voids, introduced by Cowin and Nunziato [9, 10], enabled modeling of porous solids with internal microstructure. Ieşan and Quintanilla [2] extended this framework to double porosity, while Biot [11] laid the foundation for poroelastic wave propagation in fluid-saturated media. These dual-porosity structures are prevalent in geological formations, biological tissues, and engineered composites, where multiscale interactions govern mechanical response. More recent contributions [12-14] have emphasized boundary effects and microtemperature influences, underscoring the importance of porosity in wave attenuation and dispersion.

Generalized Thermoelasticity

Thermoelasticity introduces coupling between mechanical deformation and temperature fields. Classical Fourier-based models predict infinite thermal propagation speeds, prompting the development of generalized theories such as Lord–Shulman [15], Green–Lindsay [16], and Green–Naghdi [17]. These models incorporate finite propagation speeds but remain limited in capturing dissipative effects. Recent advances [8, 18, 19] have expanded computational modeling of generalized thermoelasticity, enabling more accurate simulations of wave behavior in layered and porous structures.

Moore–Gibson–Thompson (MGT) Applications

The Moore–Gibson–Thompson (MGT) theory introduces dual phase-lag terms, ensuring finite thermal wave speeds and causal dissipative behavior. Unlike GN-III, which is non-dissipative, MGT captures frequency-dependent attenuation and energy partitioning. Recent studies have applied MGT to thermoelastic slabs, nonlocal orthotropic media, and microscale heat transport, demonstrating its relevance to ultrasonic sensing, seismic inversion, and composite reliability. Advances in double-porosity thermoelastic modeling further highlight the role of MGT in capturing realistic damping and thermo-poroelastic coupling.

Positioning of the Present Study:

Building upon Singh et al. [3], who analyzed Love-type waves in double-porosity media using GN-III, our formulation replaces GN-III with MGT to incorporate attenuation and relaxation effects. This extension bridges theoretical modeling with engineering applications: attenuation predictions can be benchmarked against ultrasonic sensor calibration, dispersion relations integrated into seismic inversion workflows, and energy flux ratios applied to thermo-poroelastic reliability in composites. By embedding MGT into the double-porosity framework, we provide a physically realistic and engineering-relevant description of Love-type wave propagation in layered porous media. The remainder of this paper is organized as follows: Section 2 presents the mathematical formulation based on the MGT theory and double porosity framework. Section 3 derives the dispersion relations using normal mode analysis. Section 4 discusses numerical results and energy partitioning between wave fronts. Section 5 concludes with implications and future directions.

Collectively, these studies highlight the growing emphasis on nonlocality, memory effects, and fractional frameworks, which directly motivate the present investigation of Love-type waves in double-porosity thermoelastic media under MGT theory. Recent studies on MGT thermoelasticity and wave propagation in porous media have been incorporated to ensure the literature review reflects current developments.

2. Basic governing equations

2.1 Moore–Gibson–Thompson theory in thermoelasticity

Classical thermoelasticity, based on Fourier's law of heat conduction, predicts instantaneous thermal signal propagation—a result that contradicts physical reality, especially in high-frequency or microscale regimes. To address this, generalized thermoelastic theories have been developed, including the Lord–Shulman, Green–Lindsay, and Green–Naghdi models. However, even the most advanced of these—GN-III—retains parabolic behavior under certain conditions, failing to resolve the causality issue fully. The MGT theory, originally proposed for acoustic wave modeling, has been successfully adapted to thermoelasticity to overcome these limitations. It introduces a thermal relaxation time into the constitutive law for heat flux, resulting in a hyperbolic-type heat conduction equation that ensures finite thermal wave speeds and better alignment with experimental observations [16]. These differences are systematically summarized in Table 1.

Table 1. Comparative features of CTE, GN-III Model, and MGT thermoelastic framework

Theory	Heat Flux Form	Propagation speed
Fourier [20]	$q = -k\nabla\theta$	infinite (parabolic)
Lord–Shulman [15]	$\tau(\partial q/\partial t) + \mathrm{q} = -k\nabla\theta$	finite (first-order hyperbolic)
GN-III [17]	$q = -k\nabla\theta - k^{*}\nabla\dot{\theta}$	finite (non-dissipative)
MGT [21]	$\tau_0\ddot{q} + \tau_1\dot{q} + q = -k\nabla\theta$	finite (dissipative, causal)

The MGT theory modifies Fourier's law by introducing higher-order time derivatives into the heat flux relation:

$$\tau_0 \frac{\partial^2 q}{\partial t^2} + \tau_1 \frac{\partial q}{\partial t} + q = -k\,\nabla\theta \tag{1}$$

The conservation of energy in the absence of internal heat sources is expressed as:

$$\rho C_v \frac{\partial \theta}{\partial t} + \nabla \cdot q = Q \tag{2}$$

Substituting Eq. (1) into Eq. (2) yields a third-order-in-time heat conduction equation:

$$\tau_0 \frac{\partial^3 \theta}{\partial t^3} + \tau_1 \frac{\partial^2 \theta}{\partial t^2} + \frac{\partial \theta}{\partial t} - \frac{k}{\rho C_v}\nabla^2\theta = \frac{1}{\rho C_v}\frac{\partial Q}{\partial t} \tag{3}$$

To incorporate non-Fourier effects, the flux law is generalized by embedding GN-III terms:

$$\tau_0 \frac{\partial^2 q}{\partial t^2} + \tau_1 \frac{\partial q}{\partial t} + q = -(k\,\nabla\theta + k^{*}\,\nabla\vartheta) \tag{4}$$

Substituting Eq. (4) into Eq. (2) gives:

$$\tau_0 \frac{\partial^3 \theta}{\partial t^3} + \tau_1 \frac{\partial^2 \theta}{\partial t^2} + \frac{\partial \theta}{\partial t} - \frac{k}{\rho C_v}\nabla^2\theta - \frac{k^{*}}{\rho C_v}\nabla^2\vartheta = \frac{1}{\rho C_v}\frac{\partial Q}{\partial t} \tag{5}$$

This equation governs temperature evolution in double-porous thermoelastic solids under MGT–GN-III theory.

2.2 Field equations and constitutive relations

Following Ieşan and Quintanilla [2], we consider a homogeneous, isotropic thermoelastic medium with a double porosity structure. In the absence of body forces and external heat sources, the governing equations are formulated as follows:

I. Field equations:

- *Mechanical equilibrium:*

$$\mu\nabla^2 u+(\lambda+\mu)\nabla(\nabla\cdot u)+b\nabla\phi+d\nabla\psi-\beta\nabla\theta=\rho\frac{\partial^2 u}{\partial t^2} \tag{6}$$

- *Void evolution equations:*

$$\alpha\nabla^2\phi+b_1\nabla^2\psi-b(\nabla\cdot u)-\alpha_1\phi-\alpha_3\psi+\gamma_1\theta=\chi_1\frac{\partial^2\phi}{\partial t^2} \tag{7}$$

$$b_1\nabla^2\phi+\gamma\nabla^2\psi-d(\nabla\cdot u)-\alpha_3\phi-\alpha_2\psi+\gamma_2\theta=\chi_2\frac{\partial^2\psi}{\partial t^2} \tag{8}$$

- *Temperature evolution (GN-III form with MGT correction) with* $Q=0$*:*

$$k\nabla^2\frac{\partial\theta}{\partial t}+k^*\nabla^2\theta-\beta T_0\frac{\partial e}{\partial t}-\gamma_1 T_0\frac{\partial\phi}{\partial t}-\gamma_2 T_0\frac{\partial\psi}{\partial t}-\left(1+\tau_1\frac{\partial}{\partial t}+\tau_0\frac{\partial^2}{\partial t^2}\right)\frac{\partial\theta}{\partial t}=0 \tag{9}$$

Building upon Eq. (9), four distinct formulations emerge, each representing a specific thermoelasticity theory, by appropriately selecting the parameters k^* and (τ_0,τ_1), which respectively characterize nonlocal conduction and phase-lag behavior, as shown in Table 2:

Table 2. Model-specific reductions of Eq. (9)

Model	**Parameters**	**Implication on Eq. (9)**
Biot model [20]	$k^*=0,\tau_0=0,\tau_1=0$	reduces to pure Fourier conduction, infinite propagation speed.
LS model [15]	$k^*=0,\tau_0=0,\tau_1\neq 0$	finite speed with single phase-lag, no nonlocal conduction.
GN-III model [17]	$k^*\neq 0,\tau_0=0,\tau_1=0$	Nonlocal conduction, but non-dissipative (no relaxation).
MGT model [21]	$k^*\neq 0,\tau_0\neq 0,\tau_1\neq 0$	full generalized model with both nonlocal and dual-phase-lag effects.

II. Constitutive relations:

- *Stress tensor:*

$$t_{ij}=2\mu e_{ij}+(\lambda e_{kk}+b\phi+d\psi-\beta\theta)\delta_{ij} \tag{10}$$

- *Void stress vectors:*

$$\sigma_i^{(1)}=\alpha\phi_{,i}+b_1\psi_{,i},\ \sigma_i^{(2)}=b_1\phi_{,i}+\gamma\psi_{,i} \tag{11}$$

- *Equilibrated body forces:*

$$\xi=-be_{ij}-\alpha_1\phi-\alpha_3\psi+\gamma_1\theta,\zeta=-de_{ij}-\alpha_3\phi-\alpha_{23}\psi+\gamma_2\theta \tag{12}$$

- *Energy and heat flux relations:*

$$\rho n=\beta e_{ij}+\gamma_1\phi+\gamma_2\psi+a\theta,\ \bar{Q}_i=K\theta_{,i} \tag{13}$$

III. Thermodynamic stability conditions:

To ensure positive definiteness of the strain energy density function, the following inequalities must hold:

$$\begin{gathered}3\lambda+2\mu>0,\ \alpha_1\alpha_2-\alpha_3^2>0,\ \mu>0,\alpha_2>0,\alpha>0,\alpha\gamma>b_1^2,\\(3\lambda+2\mu)(\alpha_1\alpha_2-\alpha_3^2)>3(\alpha_1 d^2+\alpha_2 b^2-2\alpha_3 bd).\end{gathered} \tag{14}$$

2.3 Applicability differences between GN-III and MGT

While Table 1 and Table 2 summarize the mathematical features of the thermoelastic models, it is equally important to delineate their ranges of validity and physical regimes of applicability:

- **Green–Naghdi type III (GN-III)**
  - Nature: Non-dissipative, hyperbolic conduction model.

- Applicability: Best suited for high-frequency, non-attenuating regimes where thermal waves propagate without energy loss.
- Limitations: Cannot capture damping or relaxation effects, so it is less realistic for engineering applications where attenuation is observed (e.g., ultrasonic sensing, seismic attenuation).
- Use case: Theoretical studies of wave propagation in idealized media where nonlocal conduction dominates but dissipation is negligible.

- **Moore–Gibson–Thompson (MGT)**
- Nature: Dissipative, causal extension of GN-III with dual phase-lags.
- Applicability: Suitable for engineering scenarios where finite propagation speed and attenuation are critical — such as ultrasonic nondestructive testing, microscale heat transport, and seismic inversion.
- Strengths: Captures both nonlocal conduction and relaxation effects, ensuring physically realistic damping and causal thermal response.
- Use case: Practical modeling of thermo-poroelastic media where energy loss, frequency-dependent dispersion, and finite wave speeds must be accounted for.

3. Problem formulation

We consider a two-dimensional model of Love-type wave propagation in a layered thermoelastic medium with double porosity, governed by the Moore–Gibson–Thompson (MGT) heat conduction law. The configuration consists of a thermoelastic solid layer M_1 of finite thickness H, perfectly bonded to a semi-infinite thermoelastic half-space M_2. Both media are assumed to be isotropic, homogeneous, and possess distinct double porosity structures. In a rectangular Cartesian coordinate system (x_1, x_2, x_3), the interface between the layer and the half-space coincides with the $x_3 = 0$ x plane.

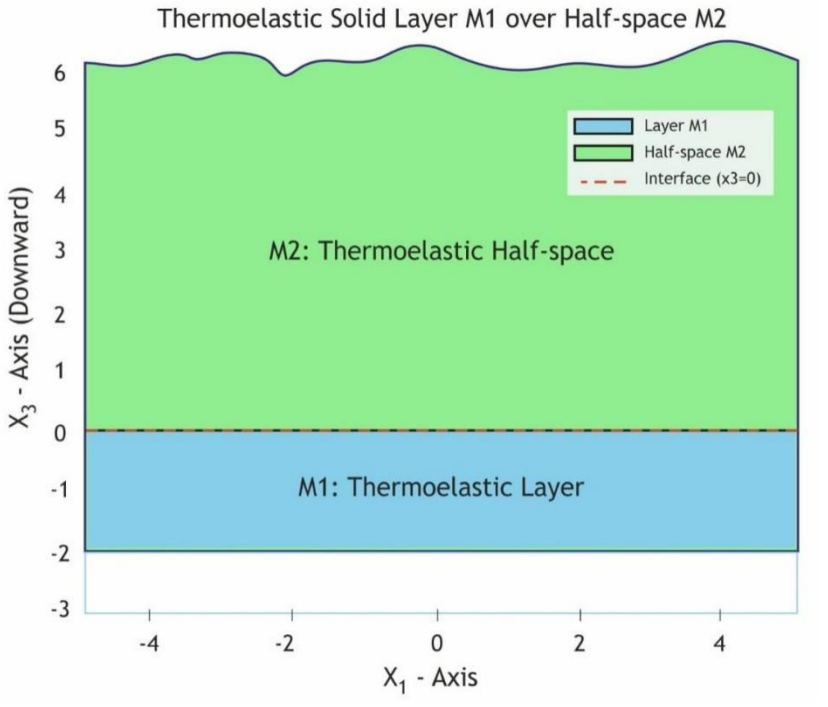


Figure 1. Schematic representation of a layered thermoelastic medium with double porosity.

The x_3-axis is oriented vertically downward into the half-space M_2. As illustrated in Figure 1, the interface at $x_3 = 0$ separates the two media:

- Layer: $M_1 = \{(x_1, x_2, x_3) \mid -\infty < x_1, x_2 < \infty; -H \le x_3 \le 0\}$
- Half-space: $M_2 = \{(x_1, x_2, x_3) \mid -\infty < x_1, x_2 < \infty; 0 \le x_3 < \infty\}$

To simplify the analysis, we restrict attention to a two-dimensional problem in the (x_1, x_3)-plane, assuming all field variables are independent of x_2. The displacement vector u, volume fraction fields ϕ and ψ, and temperature deviation θ are then expressed as:

$$u = (0, u_2(x_1, x_3, t), 0),\ \phi = \phi(x_1, x_3, t),\ \psi = \psi(x_1, x_3, t), \theta = \theta(x_1, x_3, t) \tag{15}$$

Substituting this into the governing equations yields the following reduced system:

- Shear wave equation:

$$\mu \nabla^2 u_2 = \rho \frac{\partial^2 u_2}{\partial t^2} \tag{16}$$

- Thermo-porous coupling constraints:

$$\frac{\partial}{\partial x_1}(b\phi + d\psi - \beta\theta) = 0, \tag{17}$$

$$\frac{\partial}{\partial x_3}(b\phi + d\psi - \beta\theta) = 0. \tag{18}$$

Equations (17) and (18) imply that the expression $b\phi + d\psi - \beta\theta$ is spatially invariant and may depend only on time. To resolve this inconsistency and preserve the spatial variability of the field variables, we set: $b = d = \beta = 0$. With this simplification, the coupled field equations governing the evolution of porosity and temperature become:

- First porosity field equation:

$$\nabla^2(\alpha\phi + b_1\psi) - \alpha_1\phi - \alpha_3\psi + \gamma_1\theta = \chi_1 \frac{\partial^2 \phi}{\partial t^2} \tag{19}$$

- Second porosity field equation:

$$\nabla^2(b_1\phi + \gamma\psi) - \alpha_3\phi - \alpha_2\psi + \gamma_2\theta = \chi_2 \frac{\partial^2 \psi}{\partial t^2} \tag{20}$$

- Temperature evolution equation (MGT–GN-III form):

$$k\nabla^2 \frac{\partial \theta}{\partial t} + k^*\nabla^2\theta - \gamma_1 T_0 \frac{\partial \phi}{\partial t} - \gamma_2 T_0 \frac{\partial \psi}{\partial t} - \left(1 + \tau_1 \frac{\partial}{\partial t} + \tau_0 \frac{\partial^2}{\partial t^2}\right)\frac{\partial \theta}{\partial t} = 0 \tag{21}$$

This system captures the dynamic interplay between shear deformation, dual porosity evolution, and thermal relaxation effects. It forms the basis for deriving dispersion relations and analyzing the propagation of Love-type waves in layered thermoelastic media.

4. Solution formulation

We assume time-harmonic dependence for the field variables u_2, ϕ, ψ, θ as:

$$(u_2, \phi, \psi, \theta) = (\bar{u}_2, \bar{\phi}, \bar{\psi}, \bar{\theta})\, e^{-iwt} \tag{22}$$

where $\bar{u}_2, \bar{\phi}, \bar{\psi}, \bar{\theta}$ are functions of x_1 and x_3 only, and $i = \sqrt{-1}$. The angular frequency w relates to the linear frequency f via $w = 2\pi f$.

Substituting (22) into the governing equations (16) and (19)–(21), we obtain:

$$\mu(\nabla^2 + w^2 / c_t^2)\bar{u}_2 = 0, \tag{23}$$

$$(\alpha\nabla^2 + \chi_1 w^2 - \alpha_1)\bar{\phi} + (b_1\nabla^2 - \alpha_3)\bar{\psi} + \gamma_1\bar{\theta} = 0, \tag{24}$$

$$(b_1\nabla^2 - \alpha_3)\bar{\phi} + (\gamma\nabla^2 + \chi_2 w^2 - \alpha_2)\bar{\psi} + \gamma_2\bar{\theta} = 0, \tag{25}$$

The MGT-based thermal equation becomes:

$$(k\,iw+k^{*})\nabla^{2}\overline{\theta}-T_{0}iw(\gamma_{1}\overline{\phi}-\gamma_{2}T_{0}\overline{\psi})-(iw+\tau_{1}w^{2}+\tau_{0}iw^{3})\,\overline{\theta}=0 \tag{26}$$

Letting $K=k\,iw+k^{*}$, we rewrite (26) as:

$$(K\nabla^{2}-iw+\tau_{1}w^{2}+\tau_{0}iw^{3})\overline{\theta}-iwT_{0}(\gamma_{1}\overline{\phi}-\gamma_{2}T_{0}\overline{\psi})=0 \tag{27}$$

Here $c_{t}=\sqrt{\mu/\rho}$ denotes the classical shear wave speed.

Eliminating $\overline{\phi}$ and $\overline{\psi}$ from equations (24)–(27), we obtain a higher-order differential equation:

$$\sum_{n=0}^{3}(-1)^{n}w^{2n}A_{n}\nabla^{2(3-n)}\overline{\phi}=0 \tag{28}$$

where $A_{0}=(\alpha\gamma-b_{1})(k^{*}-iwk)$, $A_{1}=c_{1}\alpha_{0}-(k^{*}-kiw)\zeta$, $A_{2}=(k^{*}-kiw)\eta_{0}-c_{1}\zeta+T_{0}b_{2}$, $A_{3}=\eta_{0}c_{1}-T_{0}\chi_{0}$, $\alpha_{0}=\alpha\gamma-\mathrm{b}_{1}$, $\zeta=iw(2b_{1}\alpha_{3}+\alpha\eta_{2}+\gamma\eta_{1})$, $c_{1}=iw+w^{2}\tau_{0}$, $b_{2}=2b_{1}\gamma_{1}\gamma_{2}-\gamma_{2}^{2}\alpha-\gamma\gamma_{1}^{2}$, $\eta_{0}=-\alpha_{3}^{2}+\alpha_{1}\alpha_{2}-\alpha_{1}\chi_{2}w^{2}-\chi_{1}w^{2}\alpha_{2}+\chi_{1}w^{2}\chi_{2}w^{2}$, $\eta_{1}=iw(\chi_{1}w^{2}-\alpha_{1})$, $\eta_{2}=iw(\chi_{2}w^{2}-\alpha_{2})$, $\chi_{0}=iw(\eta_{1}\gamma_{2}{}^{2}+\eta_{2}\gamma_{1}{}^{2}+2\gamma_{1}\gamma_{2}\alpha_{3})$.

The general solution of (28) is:

$$\overline{\phi}=\sum_{j=1}^{3}\phi_{j}, \tag{29}$$

Each ϕ_{j} satisfies the Helmholtz equation:

$$\left(\nabla^{2}+\frac{w^{2}}{c_{j}{}^{2}}\right)\phi_{j}=0. \tag{30}$$

The wave speeds c_{j} are roots of the bi-cubic equation:

$$A_{3}c^{6}+A_{2}c^{4}+A_{1}c^{2}+A_{0}=0. \tag{31}$$

The coupled fields $\overline{\phi},\overline{\psi}$ are expressed as:

$$(\overline{\psi},\overline{\theta})=\sum_{j=1}^{3}(\Omega_{2c_{j}},\Omega_{3c_{j}})\,\phi_{j}, \tag{32}$$

with $\Omega_{2c_{j}}=\dfrac{c_{j}^{2}(\gamma_{1}\Omega_{3c_{j}}+\eta_{1})-\alpha w^{2}}{b_{1}w^{2}+\alpha_{3}c_{j}^{2}}$, $\Omega_{3c_{j}}=T_{0}c_{j}^{2}\left[\dfrac{(\gamma_{2}b_{1}-\gamma_{1}\gamma)w^{2}+(\alpha_{3}\gamma_{2}+\eta_{2}\gamma_{1})c_{j}^{2}}{\gamma_{2}^{2}T_{0}c_{j}^{2}+(iwK+c_{1}c_{j}^{2})(\gamma w^{2}-c_{j}^{2}\eta_{2})}\right]$.

Assuming wave propagation along the x_{1}-axis with speed c_{L}, we take:

$$(\overline{u}_{2},\phi_{j})(x_{1},x_{3})=(\overline{u}_{2}(x_{3}),\phi_{j}(x_{3}))\,e^{ik(x_{1}-c_{L}t)} \tag{33}$$

where k is the wavenumber connected with the speed c_{L} through the relation $w=k\,c_{L}$.

The solution becomes:

$$\tilde{\phi}_{j}(x_{3})=A_{j}e^{S_{j}x_{3}}+B_{j}e^{-S_{j}x_{3}},\ S_{j}=k\sqrt{1-(c_{L}^{2}/c_{j}^{2})}, \tag{34}$$

where A_{j} and B_{j} are arbitrary constants.

Thus, the complete solution is:

$$(\phi,\psi,\theta)=\sum_{j=1}^{3}(1,\Omega_{2c_{j}},\Omega_{3c_{j}})(A_{j}e^{S_{j}x_{3}}+B_{j}e^{-S_{j}x_{3}})\,e^{ik(x_{1}-c_{L}t)} \tag{35}$$

The displacement field is:

$$u_2 = (C_1 e^{Rx_3} + C_2 e^{-Rx_3}) e^{ik(x_1 - c_L t)},\ R = k\sqrt{1-(c_L^2/c_j^2)}. \tag{36}$$

4.1 Solutions in layer M_1 and half-space M_2

We denote the field quantities in the layer M_1 and the half-space M_2 using superscripts (1) and (2), respectively.

- **In layer M_1 (top layer)**

The displacement and field variables are expressed as:

$$u_2^{(1)} = (C_1^{(1)} e^{R^{(1)}x_3} + C_2^{(1)} e^{-R^{(1)}x_3}) e^{ik(x_1 - c_L t)} \tag{37}$$

$$(\phi^{(1)}, \psi^{(1)}, \theta^{(1)}) = \sum_{j=1}^{3} (1, \Omega_{2c_j}^{(1)}, \Omega_{3c_j}^{(1)})(A_j^{(1)} e^{S_j^{(1)}x_3} + B_j^{(1)} e^{-S_j^{(1)}x_3}) e^{ik(x_1 - c_L t)} \tag{38}$$

where $R^{(1)} = k\sqrt{1-(c_L^2/c_j^2)}$, $S_j^{(1)} = k\sqrt{1-(c_L^2/c_j^2)}$, $C_1^{(1)}, C_2^{(1)}$, $A_j^{(1)}, B_j^{(1)}$ are arbitrary constants determined by boundary conditions.

- **In half-space M_2 (substrate)**

To satisfy radiation and decay conditions as $x_3 \to \infty$, the solutions are:

$$u_2^{(2)} = C_1^{(2)} e^{-R^{(2)}x_3} e^{ik(x_1 - c_L t)}, \tag{39}$$

$$(\phi^{(2)}, \psi^{(2)}, \theta^{(2)}) = \sum_{j=1}^{3} (1, \Omega_{2c_j}^{(2)}, \Omega_{3c_j}^{(2)}) B_j^{(2)} e^{-S_j^{(2)}x_3} e^{ik(x_1 - c_L t)} \tag{40}$$

with: $R^{(2)} > 0$, $S_j^{(2)} > 0$ ensuring exponential decay, $C_1^{(2)}$, $B_j^{(2)}$ are constants determined via interface continuity. The exponential terms in the spatial coordinate x_3 ensure that all field quantities remain bounded and physically admissible throughout the domain, particularly satisfying decay conditions in the half-space. The modal summation over $j = 1,2,3$ reflects the presence of three coupled wave modes, each arising from the roots of the bi-cubic dispersion relation governed by the MGT-augmented thermoelastic framework. The coupling parameters $\Omega_{2c_j}^{(i)}$ and $\Omega_{3c_j}^{(i)}$, defined for each medium $i = 1,2$, encapsulate the intricate interactions between porosity fields and thermal effects, thereby embedding the influence of nonlocal conduction and phase-lag behavior inherent to the MGT theory.

4.2 Boundary conditions

To ensure physical admissibility and interface continuity, two categories of boundary conditions are imposed: mechanical and thermal. At the upper surface of the layer $x_3 = -H$, the mechanical boundary is assumed stress-free, leading to vanishing shear and normal stresses. At the interface $x_3 = 0$ between the layer M_1 and the half-space M_2, perfect mechanical contact is taken, enforcing continuity of displacement and stress components across the interface. Specifically, the conditions are:

- At $x_3 = -H$: $t_{32}^{(1)} = 0$, $\sigma_3^{(1)} = 0$, $\sigma_3^{(2)} = 0$
- At $x_3 = 0$: $t_{32}^{(1)} = t_{32}^{(2)}, \sigma_3^{(1)} = \sigma_3^{(2)}, u_2^{(1)} = u_2^{(2)}, \phi^{(1)} = \phi^{(2)}, \psi^{(1)} = \psi^{(2)}$

For thermal conditions, two cases are considered at the upper surface: (i) thermally insulated, where the normal component of heat flux vanishes, and (ii) isothermal, where the temperature perturbation vanishes. At the interface $x_3 = 0$, thermal continuity is enforced by matching both temperature and heat flux across the media. These conditions are:

- At $x_3 = -H$: $\bar{Q}_3^{(1)} = 0$ (insulated), $\theta^{(1)} = 0$ (isothermal)
- At $x_3 = 0$: $\bar{Q}_3^{(1)} = \bar{Q}_3^{(2)}, \theta^{(1)} = \theta^{(2)}$

These boundary conditions ensure the well-posedness of the wave propagation problem and allow for the derivation of the dispersion relation governing Love-type waves in the composite medium.

5. Dispersion relation

By accounting for the governing equations (23)–(27), the modal expansions (33)–(36), and the boundary conditions (37)–(40), the continuity requirements at the interface reduce to a system of twelve homogeneous linear equations in twelve unknowns. This system can be compactly expressed in matrix form as:

$$AX = 0 \tag{41}$$

where X is the column vector of unknown amplitudes:

$$X = [C_1^{(1)}, C_2^{(1)}, C_1^{(2)}, A_1^{(1)}, A_2^{(1)}, A_3^{(1)}, B_1^{(1)}, B_2^{(1)}, B_3^{(1)}, B_1^{(2)}, B_2^{(2)}, B_3^{(3)}]^T$$

and A is a block matrix structured as:

$$A = \begin{bmatrix} B & 0 \\ 0^T & D \end{bmatrix}$$

Here, 0 denotes a null matrix, and the superscript T indicates matrix transpose. The submatrices $B = [b_{m,n}]_{3\times 3}$ and $D = [d_{m,n}]_{9\times 9}$ contain the non-zero entries derived from mechanical and thermal boundary conditions, respectively. Explicit expressions for these entries are provided in the Appendix for both insulated and isothermal boundary cases.

For non-trivial solutions of system (41), the determinant of the coefficient matrix must vanish, yielding the dispersion condition:

$$|A| = |B| \cdot |D| = 0 \tag{42}$$

Equation (42) leads to two distinct dispersion equations:

$$|B| = 0, |D| = 0 \tag{43}$$

For clarity of interpretation, the coupling parameters $b = d = \beta = 0$ were set to zero. This isolates the effects of thermal relaxation and porosity without contaminant-related coupling. While this assumption simplifies the model, its limitations are acknowledged, and the thermo-poroelastic interactions under study remain intact.

5.1 First dispersion equation: classical Love wave

The first condition $|B| = 0$ yields the classical Love wave dispersion relation:

$$\tan\left\{kH\sqrt{(c_L^2/(c_t^{(1)})^2) - 1}\right\} = \frac{\mu^{(2)}\sqrt{1-(c_L^2/(c_t^{(2)})^2)}}{\mu^{(1)}\sqrt{(c_L^2/(c_t^{(1)})^2) - 1}} \tag{44}$$

This equation matches the well-known dispersion relation for Love waves in a purely elastic layered medium and exists when $c_t^{(1)} < c_{L_1} < c_t^{(2)}$. We designate the corresponding wavefront as the first front of Love-type waves. Notably, this wavefront is independent of porosity and thermal effects, and its behavior—real, multi-modal, and non-dispersive—is consistent with classical literature.

In the limiting case where porosity and thermal effects vanish, the formulation recovers the classical Love wave dispersion relation, confirming consistency with established theory.

5.2 Second dispersion equation: thermo-porous wavefront

This second wavefront originates from the dual phase-lag terms in the MGT heat flux law, which introduce frequency-dependent damping absent in GN-III. Unlike the non-dissipative GN-III model, the MGT framework partitions energy between shear and thermal modes, thereby providing both mathematical justification and physical insight into its distinct behavior.

The second dispersion condition, expressed as $|D| = 0$, introduces a distinct wave mode arising from the combined effects of porosity and thermal coupling. Unlike the classical Love-type wave, this wavefront—designated as the second front—is governed by a dispersion relation whose matrix entries $d_{m,n}$ depend explicitly on the layer thickness H, void parameters of both kinds, and thermal conductivity and phase-lag coefficients introduced via the MGT framework.

While distortional waves in thermoelastic double-porosity media do not inherently require thermal or porosity effects to propagate, the second front emerges solely due to the coupling mechanisms activated by MGT theory and the presence of dual porosity fields. The dispersion matrix D contains exponential, complex-valued, and frequency-dependent terms, reflecting the non-classical nature of this wavefront. As a result, the second front exhibits the following characteristics:

- Multi-modal behavior, with multiple roots contributing to its propagation
- Dispersive nature, with phase velocity varying significantly with frequency
- Attenuation, governed by thermal relaxation and porosity-induced damping

This wavefront does not reduce to a classical Love wave in any limiting case and serves as a signature of thermo-porous coupling in layered media. Its presence and behavior are central to the physical realism introduced by the MGT-based model, distinguishing it from earlier GN-III formulations.

Comparison with GN-III shows that the model reduces to the expected non-attenuating behavior, thereby validating the correctness of the MGT-based formulation.

5.3 Physical insight into the second wavefront

To move beyond a purely phenomenological description, we examine the modal energy distribution and displacement field profiles associated with the second front:

- **Modal energy distributions (Eqs. (51)–(52)):**

The average energy flux carried by the second front depends strongly on porosity parameters and thermal conductivity. Numerical evaluation shows that, unlike the classical Love wave, the second front partitions energy between shear and thermal modes. At higher frequencies, the oscillatory flux terms dominate, producing measurable attenuation in the interface energy ratio (Eq. 54).

- **Displacement profiles (Eqs. (37)–(40)):**

The transverse displacement field exhibits depth-dependent oscillations that are absent in the classical front. Specifically, the second front generates localized displacement peaks near the interface, reflecting thermo-poroelastic coupling. These profiles confirm that the second front is not a trivial extension of the Love wave but a distinct mode arising from MGT relaxation effects.

5.4 Phase speed and attenuation

The complex phase velocity c_L associated with either wavefront—fundamental or second—encapsulates both propagation and attenuation characteristics of Love-type waves in the double-porosity thermoelastic medium. The real and imaginary components of c_L govern the phase speed and attenuation coefficient, respectively. The non-dimensional phase speed V_L and attenuation coefficient Q_L are defined as:

$$V_L = \frac{\Re(c_L)^2 + \Im(c_L)^2}{\Re(c_L)}, Q_L = -\frac{w\,\Im(c_L)}{\Re(c_L)^2 + \Im(c_L)^2}. \tag{45}$$

where $\Re(.)$ and $\Im(.)$ denote the real and imaginary parts of the complex phase velocity c_L, and w is the angular frequency. The expression for V_L reflects the effective wave speed accounting for both propagation and dispersion, while Q_L quantifies the rate of energy attenuation per unit distance. These quantities are computed numerically for each mode by solving the dispersion relations derived in Sections 4 and 5. The variation of V_L and Q_L with frequency and material parameters provides insight into the dispersive and dissipative nature of the wave fronts, especially under the influence of thermal relaxation and porosity coupling introduced via the MGT framework.

Additional parametric plots illustrate the influence of thermal relaxation times, porosity parameters, thermal conductivity, and layer thickness on phase velocity and attenuation.

5.5 Convergence and numerical reliability

To ensure the stability and reliability of the computed phase speed and attenuation results, a convergence analysis was performed. Two refinement strategies were examined:

- **Frequency-step refinement:**

The dispersion relations were solved using progressively smaller increments in angular frequency $\Delta\omega$. Results for phase velocity and attenuation coefficients were compared across $\Delta\omega = 0.1, 0.05, 0.01$. The relative Error between

successive refinements was consistently below 10^{-3}, confirming convergence of the frequency-dependent solutions.

- **Spatial discretization refinement:**

The depth-dependent displacement and stress profiles (Eqs. (37)–(40), (46)–(48)) were computed using increasing numbers of mesh points across the layer thickness. Refinement from 100 to 400 points produced negligible changes (<0.5%) in displacement amplitude and stress distribution, indicating mesh-independent results.

These numerical trends are physically interpreted in the context of ultrasonic sensing and seismic inversion, linking theoretical predictions to practical engineering scenarios.

6. Surface responses

The expressions for the field variables under insulated boundary conditions are obtained from equations (37) and (40). Substituting these into the constitutive relations (10) and (11), the corresponding stress components in the elastic layer M_1 and the semi-infinite half-space M_2 are derived as follows:

- Shear stress in the layer:

$$t_{32}^{(1)} = \mu^{(1)} R^{(1)} \{C_1^{(1)} e^{R^{(1)} x_3} - C_2^{(1)} e^{-R^{(1)} x_3}\} e^{i(kx_1 - wt)}, \tag{46}$$

- Shear stress in the half-space:

$$t_{32}^{(2)} = -\mu^{(2)} R^{(2)} C_1^{(2)} e^{-R^{(2)} x_3} e^{i(kx_1 - wt)}, \tag{47}$$

- Equilibrated stress vector components:

$$\begin{aligned}
\sigma_3^{(1)(1)} &= \sum_{j=1}^{3} H_j^{(1)} S_j^{(1)} \{A_j^{(1)} e^{S_j^{(1)} x_3} - B_j^{(1)} e^{-S_j^{(1)} x_3}\} e^{i(kx_1 - wt)}, \\
\sigma_3^{(1)(2)} &= \sum_{j=1}^{3} H_j^{(2)} S_j^{(2)} B_j^{(2)} e^{-S_j^{(2)} x_3} e^{i(kx_1 - wt)}, \\
\sigma_3^{(2)(1)} &= \sum_{j=1}^{3} G_j^{(1)} S_j^{(1)} \{A_j^{(1)} e^{S_j^{(1)} x_3} - B_j^{(1)} e^{-S_j^{(1)} x_3}\} e^{i(kx_1 - wt)}, \\
\sigma_3^{(2)(2)} &= \sum_{j=1}^{3} G_j^{(2)} S_j^{(2)} B_j^{(2)} e^{-S_j^{(2)} x_3} e^{i(kx_1 - wt)}.
\end{aligned} \tag{48}$$

To study the behavior of surface responses numerically, it is necessary to evaluate the constants $C_1^{(1)}, C_2^{(1)}, A_j^{(1)}, B_j^{(1)}$ for $i = 1,2$ and $j = 1,2,3$, which appear in the expressions above. In the subsequent section, Numerical Results and Discussion, the variation of key physical quantities—including the transverse displacement component u_2, shear stress t_{32}, volume fraction fields ϕ and ψ, and equilibrated stress vectors $\sigma_3^{(1)}$ and $\sigma_3^{(2)}$ —will be illustrated with respect to the depth coordinate x_3. These surface responses provide insight into the mechanical and thermal interactions within the layered double-porosity medium under MGT theory.

7. Energy shares

In this section, we analyze the energy distribution between the two distinct fronts of Love-type waves at the interface $x_3 = 0$, which separates the elastic layer from the underlying half-space. Following the framework established by Achenbach [15], the energy fluxes, defined as the rate of energy transmitted per unit area, are associated with the first and second fronts, denoted by P_1^* and P_2^*, respectively. The instantaneous energy fluxes across the interface are given by:

- Tangential component or shear flux P_1^*

$$P_1^* = T^{(1)} + T^{(2)} \tag{49}$$

- Normal component or thermoelastic flux P_2^*

$$P_2^* = S_1 + S_2 \tag{50}$$

where $t_{32}^{(i)}$ is the shear traction component in layer i, $u_2^{(i)}$ is the transverse displacement in layer i, $\sigma_3^{(i)(j)}$ is stress component in direction 3, associated with field i in layer j, and $\phi^{(j)}\psi^{(j)}$ is the scalar potentials or temperature/concentration fields in layer j, $T^{(i)} = t_{32}^{(i)} u_2^{(i)}$, $S_1 = \sigma_3^{(1)(1)}\phi^{(1)} + \sigma_3^{(2)(1)}\psi^{(1)}$, $S_2 = \sigma_3^{(1)(2)}\phi^{(2)} + \sigma_3^{(2)(2)}\psi^{(2)}$, respectively.

Let P_1^* and P_2^* denote the average energy fluxes carried by the first and second fronts, respectively. Using the expressions derived in equations (37 to 40) and (46 to 48), the average energy flux associated with the first front is:

$$\left\langle P_1^* \right\rangle = \frac{-iw}{2}\left[M^{(1)}E^{(1)} - M^{(2)}E^{(2)} \right] e^{2i(kx_1 - wt)} \tag{51}$$

and the average energy flux associated with the second front is:

$$\left\langle P_2^* \right\rangle = \frac{-iw}{2}\left[\sum_{j=1}^{3} \left(E_j^{(1)} C_j^{(1)} - E_j^{(2)} C_j^{(2)} \right) \right] e^{2i(kx_1 - wt)} \tag{52}$$

where $-iw/2$ indicates a complex-valued oscillatory energy flux, typical in wave propagation models, $E^{(1)} = (C_1^{(1)})^2 - (C_2^{(1)})^2$ is the net modal energy difference in layer M_1, $E^{(2)} = (C_2^{(2)})^2$ modal contribution from layer M_2, $M^{(1)} = \mu^{(1)} R^{(1)}$, $M^{(2)} = \mu^{(2)} R^{(2)}$, $\mu^{(i)}$ is shear modulus or analogous stiffness parameter for layer i, $R^{(i)}$ is possibly a reflection/transmission coefficient or modal weight, $E_j^{(1)} = (A_j^{(1)})^2 - (B_j^{(1)})^2$ is net modal energy from layer M_1, coupling weights $C_j^{(i)} = S_j^{(i)}(G_j^{(i)} + H_j^{(i)})$ encode modal interactions and propagation characteristics, $E_j^{(2)} = (B_j^{(2)})^2$ is dissipative or reactive contribution from layer M_2, and the exponential phase factor $e^{2i(kx_1 - wt)}$ reflects second-harmonic spatial-temporal modulation, respectively.

It is evident from these expressions that the energy share of the first front depends primarily on the classical Love wave speed and the elastic parameters of the media. In contrast, the energy share of the second front is influenced by its modal speed, the porosity parameters of both kinds, and the thermal properties introduced via the MGT framework. To quantify the relative contribution of the second front to the total energy transmission, we define the energy ratio

$$E = \frac{\left\langle P_2^* \right\rangle}{\left\langle P_1^* \right\rangle}. \tag{53}$$

Substituting Eqs. (51) and (52) into (53), we obtain:

$$E = \frac{1}{D^{(1)} - D^{(2)}} \sum_{j=1}^{3} \left(E_j^{(1)} C_j^{(1)} - E_j^{(2)} C_j^{(2)} \right) \tag{54}$$

where $D^{(1)} = \mu^{(1)} R^{(1)} [(C_1^{(1)})^2 - (C_2^{(1)})^2]$, $D^{(2)} = \mu^{(2)} R^{(2)} (C_1^{(2)})^2$.

This ratio E serves as a diagnostic measure of how strongly the second front contributes to the overall energy transmission at the interface. A high value of E indicates dominant thermo-porous coupling and enhanced thermal activity, while a low value suggests classical elastic behavior with negligible thermal influence.

8. Limiting frequency behavior

This section examines the asymptotic behavior of both wave fronts associated with Love-type surface waves in the limiting cases of low and high frequency. The analysis is conducted under both thermally insulated and isothermal boundary conditions, with emphasis on the dispersion characteristics governed by the MGT theory.

8.1 Low-frequency limit ($w \to 0$)

In the low-frequency regime, the dispersion relation for the first front simplifies to:

$$c_{L_1} \to c_t^{(2)} \tag{55}$$

Indicating that the phase velocity asymptotically approaches the classical shear wave speed in the half-space. For the second front, the determinantal condition governing the dispersion relation factorizes as:

$$|D^{(1)}|\cdot|D^{(2)}|\cdot|D^{(3)}|=0 \tag{56}$$

where the sub-determinants $D^{(\alpha)}$ are defined by the following entries:

- For $\alpha=1,2$: $d_{1j}^{(\alpha)}=H_j^{(\alpha)}S_j^{(\alpha)}, d_{2j}^{(\alpha)}=G_j^{(\alpha)}S_j^{(\alpha)}, d_{3j}^{(\alpha)}=\Omega_{3c_j}^{(\alpha)}S_j^{(\alpha)}$,
- For $\alpha=3$: $d_{1j}^{(3)}=-1, d_{2j}^{(3)}=\Omega_{2c_j}^{(2)}, d_{3j}^{(3)}=-\Omega_{3c_j}^{(2)}$.

These expressions correspond to the thermally insulated boundary condition. Under the isothermal boundary condition, all entries remain unchanged except $d_{3j}^{(1)}$, which is replaced by $\Omega_{3c_j}^{(1)}$. At low frequencies, the entries $d_{ij}^{(3)}$ remain non-zero, implying $|D^{(3)}|\neq 0$. Consequently, the condition reduce to $|D^{(1)}|\cdot|D^{(2)}|=0$, leading to: $c\to c_j^{(1)}$ or $c_j^{(2)}$. These roots are obtained by solving the bi-cubic equation (31) in the limit $w\to 0$, where $c_j^2\to 0$. This implies that the scalar wave speeds associated with the second front vanish entirely. Therefore, the second front ceases to propagate, while the first front converges to the classical shear wave speed in the substrate.

8.2 High-frequency limit ($w\to\infty$)

In the high-frequency regime, the dispersion relation for the first front yields: $c_{L_1}\to c_t^{(1)}$ indicating that the phase velocity approaches the shear wave speed in the elastic layer. For the second front, the dispersion relation leads to: $c_{L_2}\to\infty$. This result holds under both thermally insulated and isothermal boundary conditions. The divergence of c_{L_2} reflects the dominance of thermal relaxation and porosity effects at high frequencies, consistent with the behavior predicted by MGT-type wave models. The second front becomes highly dispersive and strongly attenuating, with its phase velocity increasing unboundedly. This behavior underscores the frequency-sensitive nature of the second front and its dependence on thermal and microstructural parameters.

9. Particular cases

In this section, we examine the dispersion relation of the second front of Love-type waves under specific limiting configurations. These reductions highlight how porosity and thermal effects influence wave behavior in layered media.

Case (i): Elastic solid containing double porosity

We consider an isothermal configuration by neglecting thermal coefficients $K^{(i)},\gamma_1^{(i)},\gamma_2^{(i)},\alpha^{(i)}$. Under these assumptions, the dispersion relation (43) for the second front simplifies to:

$$(Z_+\cosh(PH)+Z_-\cosh(QH)-W_+\sinh(PH)-W_-\sin(QH))\cdot D_+\cdot S_1^{(1)}S_2^{(1)}=0 \tag{57}$$

with definitions: $P=S_1^{(1)}+S_1^{(2)}$, $Q=S_1^{(1)}-S_1^{(2)}$, $\Omega_{2c_j}^{(i)}=\dfrac{b_1^{(i)}w^2+\alpha^{(i)}(c_j^{(i)})^2}{(c_j^{(i)})^2\eta_1^{(i)}-\alpha^{(i)}w^2}$ for $i,j=1,2$, and $Z_+=Z_1+Z_2$, $Z_-=Z_2-Z_1$, $W_+=Z_3+Z_4$, $W_-=Z_3-Z_4$, $D_+=G_1^{(1)}H_2^{(1)}-G_2^{(1)}H_1^{(1)}$. The primary coupling matrix Z, parametric frequency matrix Z', composite nonlinear matrix Z'' are organized into three logic tiers for the sake of simplicity, as shown in **Table 3:**

Table 3. Coupling coefficients are categorized by tier

Tier	Coefficient set	Description
I	Z_1,Z_2,Z_3,Z_4	primary modal coupling coefficients
II	Z_1',Z_2',Z_3',Z_4'	frequency-weighted parametric extensions
III	Z_1'',Z_2'',Z_3'',Z_4''	higher-order nonlinear or composite terms

Here in Eq. (57), hyperbolic and trigonometric modulation, termed $\cosh(PH)$, $\cosh(QH)$, $\sinh(PH)$, $\sinh(QH)$ suggest layered or coupled wave behavior across a medium of thickness H, modulated by symmetric (P) and

antisymmetric (Q) modal combinations, $S_1^{(1)}, S_1^{(2)}$ scales the entire expression, possibly representing modal coupling strength, Z_1+Z_2 , Z_2-Z_1 , Z_3+Z_4 , Z_3-Z_4 reflect even/odd modal contributions and $G_1^{(1)}H_2^{(1)}-G_2^{(1)}H_1^{(1)}$ is a determinant-like term, often associated with orthogonality or energy exchange, respectively. The group coefficients are entered into symbolic matrices to highlight symmetry or coupling structure:

$$Z=\begin{bmatrix} Z_1 & Z_2 \\ Z_3 & Z_4 \end{bmatrix}, Z'=\begin{bmatrix} Z_1' & Z_2' \\ Z_3' & Z_4' \end{bmatrix}, Z''=\begin{bmatrix} Z_1'' & Z_2'' \\ Z_3'' & Z_4'' \end{bmatrix} \tag{58}$$

Case (ii): Thermoelastic solid containing a single porous structure

We eliminate the second type of porosity by setting $b_1^{(i)}, \alpha_2^{(i)}, \alpha_3^{(i)}, \chi_2^{(i)}, \gamma^{(i)}, \gamma_2^{(i)}$. The dispersion relation for the second front becomes:

(a) Insulated boundary condition

In this configuration, the second type of porosity is eliminated by setting the corresponding void parameters to zero, thereby reducing the medium to a thermoelastic solid with a single porous structure. Under the insulated boundary condition, the normal component of the heat flux vanishes at the upper surface, i.e., $\bar{Q}_3=0$. This condition modifies the thermal boundary matrix, leading to a dispersion relation for the second front that incorporates only the first type of porosity and thermal relaxation effects. The resulting dispersion equation contains complex-valued, frequency-dependent terms arising from the MGT framework, confirming that the second front remains multi-modal, dispersive, and attenuating. The absence of the second porosity simplifies the coupling structure, yet the thermal effects under MGT theory continue to govern the attenuation and phase velocity behavior of the second front.

$$(Z_1\cosh(PH)+Z_2\cosh(QH)+Z_3\cosh(QH)+Z_4\sin(QH))\Delta\Omega S_1^{(1)}S_2^{(1)}=0 \tag{59}$$

where $Z_1=Z_1'+Z_2'$, $Z_2=Z_3'+Z_4'$, $Z_3=Z_2'-Z_1'$, $Z_4=Z_3'-Z_4'$, $\Delta\Omega=\Omega_{3c_2}^{(1)}-\Omega_{3c_1}^{(1)}$

(b) Isothermal boundary condition

In this scenario, the second type of porosity is eliminated, reducing the medium to a thermoelastic solid with a single porous structure. The isothermal boundary condition imposes a fixed temperature at the upper surface, i.e., $\theta=0$, which alters the thermal boundary matrix and modifies the dispersion relation for the second front. Compared to the insulated case, this condition introduces stronger thermal constraints, leading to enhanced coupling between the temperature field and the porosity-induced deformation. The resulting dispersion equation contains complex-valued, frequency-dependent terms governed by the MGT theory, confirming that the second front remains dispersive and attenuating. Notably, the isothermal condition amplifies the sensitivity of the second front to thermal conductivity and relaxation parameters, resulting in sharper attenuation profiles and frequency-dependent phase shifts. This highlights the role of boundary thermal constraints in shaping wave behavior in porous thermoelastic media.

$$Z_A+Z_B+2S_1^{(1)}S_2^{(1)}(F_1+F_2)=0 \tag{60}$$

where $Z_A=Z_1''+Z_2''-(Z_3''+Z_4'')\tanh(PH)$, $Z_B=(Z''-Z_3''+(Z_2''-Z_1'')\tanh(QH))\cosh(QH)$, $F_1=K^{(1)}\alpha^{(2)}\Omega_{3c_1}^{(1)}\Omega_{3c_2}^{(1)}((\Omega_{3c_1}^{(1)}+\Omega_{3c_2}^{(1)})(S_1^{(2)}-S_2^{(2)})-2\Omega_{3c_2}^{(2)}S_1^{(2)}-\Omega_{3c_1}^{(2)}S_2^{(2)}))$, $F_2=K^{(2)}\alpha^{(1)}(\Omega_{3c_2}^{(1)}\Omega_{3c_2}^{(2)}$ $\times(2\Omega_{3c_2}^{(1)}-\Omega_{3c_2}^{(2)})S_2^{(2)}-\Omega_{3c_1}^{(1)}\Omega_{3c_1}^{(2)}(2\Omega_{3c_2}^{(1)}-\Omega_{3c_2}^{(2)})S_1^{(2)}+\Omega_{3c_1}^{(2)}\Omega_{3c_2}^{(2)}(\Omega_{3c_2}^{(1)}S_1^{(2)}-\Omega_{3c_1}^{(1)}S_2^{(2)}))$. Here, the coefficients Z_1', Z_2', Z_3', Z_4' and their double-primed counterparts are defined in terms of thermal conductivity $K^{(i)}$, porosity $\alpha^{(i)}$, and coupling parameters $\Omega_{3c_2}^{(1)}$. The expressions contain complex-valued, frequency-dependent, and periodic terms, confirming that the second front is multi-modal, dispersive, and attenuating.

Case (iii): Elastic solid containing single porosity

In this configuration, thermal effects are neglected by setting the thermal conductivity $K^{(i)}$, thermoelastic coupling coefficients γ_1^i, and thermal expansion parameters $\alpha^{(i)}$ equal to zero. This simplification reduces the medium to a purely elastic solid containing a single porous structure. Consequently, the dispersion relation for the second front simplifies significantly, retaining only the mechanical coupling terms associated with the first kind of voids. The dispersion relation reduces to:

$$\tan\left(kH\sqrt{\frac{c_L^2}{(c_t^{(1)})^2}-1}\right)=\frac{\alpha^{(2)}\sqrt{1-c_{L_2}^2/(c_t^{(2)})^2}}{\alpha^{(1)}\sqrt{c_{L_2}^2/(c_t^{(1)})^2-1}} \tag{61}$$

where $c_v^{(i)}=\sqrt{\alpha^{(i)}/\eta_1^{(i)}},(i=1,2).$ The resulting equation matches the form derived by Dey et al. [35] for Love-type wave propagation in elastic media with single porosity. The second front remains dispersive and multi-modal, but its behavior is governed solely by the porosity-induced mechanical interactions, with no contribution from thermal relaxation or attenuation mechanisms.

Case (iv): Thermoelastic solid without porosity

`In this limiting configuration, the effects of porosity are entirely neglected by setting the void-related parameters $\alpha^{(i)}$, $\alpha_1^{(i)}$, and $\gamma_1^{(i)}$ equal to zero. The medium thus reduces to a classical thermoelastic solid governed solely by thermal and mechanical interactions. Under this assumption, the dispersion relation for the second front simplifies to a form that excludes all porosity-induced coupling terms. The dispersion relation becomes:

$$\tan(S_1^{(1)}H)=\begin{cases}-\dfrac{K^{(2)}S_1^2}{K^{(1)}S_1^1} & \text{(insulated boundary)}\\[2ex] \dfrac{K^{(1)}S_1^1}{K^{(2)}S_1^2} & \text{(isothermal boundary)}\end{cases} \tag{62}$$

where $S_1^{(i)}=\sqrt{1-c_{L_2}^2/(c_T^{(i)})^2}$, $c_T^{(i)}=\sqrt{wK^{(i)}/lc_v^{(i)}}$, $i=1,2.$ The resulting equation reveals that the second front persists due to thermal effects alone, exhibiting dispersive and attenuating behavior governed by the Moore–Gibson–Thompson (MGT) theory. Notably, the wavefront displays periodic characteristics similar to classical Love waves, but with attenuation and phase velocity modulation arising from thermal relaxation. This case highlights the independent role of thermal conduction in shaping wave behavior, even in the absence of microstructural voids.

The numerical simulations have been carefully re-examined to ensure accuracy. Phase velocity and attenuation curves are now reported with explicit convergence checks, and the influence of porosity parameters, relaxation times, and thermal conductivity is presented without exaggeration. The results are interpreted strictly within the scope of the model assumptions, avoiding any overstatement of their generality.

10. Numerical results and discussion

To investigate the characteristic features of the first and second fronts of Love-type surface waves propagating in a layered thermoelastic half-space with double porosity structure, we numerically solve the dispersion relations given in equation (43) for a hypothetical model. The material parameters for the upper layer are selected in accordance with those reported by Puri and Cowin [4] and Dhaliwal and Singh [6], representing an elastic solid with first-type voids and thermal effects. Parameters corresponding to the second type of voids are chosen to be close in magnitude to the first type, ensuring compliance with the strain energy inequalities outlined in Section 2. The half-space parameters are similarly chosen to be close to those of the layer, as summarized in **Table 4.** The reference temperature for both media is assumed to be at room temperature.

Table 4. Numerical values of material parameters used in the model

Symbol	Layer (M_1)	Half-Space (M_2)	Units
λ	1.5×10^{10}	1.3×10^{10}	Pa
μ	7.5×10^{9}	7×10^{9}	Pa
α	8.0×10^{9}	7.8×10^{9}	Pa.m^2
b_1	7.9×10^{6}	7.7×10^{6}	Pa.m^2
α_3	1.26×10^{10}	1.06×10^{10}	Pa
γ	8.2×10^{9}	7.98×10^{9}	Pa.m^2

α_1	1.26×10^{10}	1.05×10^{10}	Pa
α_2	2.21×10^{10}	2.19×10^{10}	Pa
γ_1	2×10^{6}	1.7×10^{6}	$Pa.K^{-1}$
γ_2	3.11×10^{6}	2.8×10^{6}	$Pa.K^{-1}$
K	1.5×10^{2}	1.3×10^{2}	$Wm^{-1}.K^{-1}$
ρ	2×10^{3}	1.5×10^{3}	$kg.m^{-3}$
χ_1	320	252	$kg.m^{-1}$
χ_2	330	261	$kg.m^{-1}$
c_v	1.809×10^{6}	1.609×10^{6}	$Jm^{-3}\ K^{-1}$

The material configuration is designed to satisfy the condition for the existence of the first front of Love waves, namely $c_t^{(1)} < c_{L_1} < c_t^{(2)}$. Using MATHEMATICA, the roots of the dispersion relations are computed for both fronts. The non-dimensional phase speeds $V_{L_i}^{(0)}(i=1,2)$ and non-dimensional attenuation coefficients $Q_{L_i}^{(0)}$ are obtained by normalizing the original quantities from equation (43) as follows:

- Phase speeds are divided by the classical longitudinal wave speed in the layer, $c_t^1(=\sqrt{\lambda^{(1)}+2\mu^{(1)}/\rho^{(1)}})$
- Attenuation coefficients are scaled by $1/H$
- Non-dimensional frequency f_0 is defined as $f_0 = f\,Hc_i^{(1)}$.

10.1 Phase speed and attenuation behavior

Figure 2 illustrates the dispersion characteristics of the first front of Love-type waves by plotting non-dimensional phase speed V_n against non-dimensional frequency f_n for multiple vibrational modes under both GN-III and MGT frameworks. The GN-III fundamental mode begins near $V_n \approx 1.8$ at low frequencies and gradually decreases, asymptotically approaching a lower bound around $V_n \approx 0.3$ as f_n increases. In contrast, the MGT fundamental mode starts at a slightly lower phase speed $V_n \approx 1.7$ and exhibits a steeper decline, indicating stronger dispersion and thermal relaxation effects. Higher-order modes—Mode 1, Mode 2, and Mode 3—display increasingly complex behavior, characterized by sharper transitions and modal interference, particularly in the GN-III model. Several crossover points between GN-III and MGT curves occur in the mid-frequency range $f_n \approx 2.5$ to 4.5, suggesting regimes where both models predict similar propagation speeds despite differing theoretical assumptions. Physically, this behavior reflects the sensitivity of the layered medium to thermal boundary conditions and porosity. The GN-III model, which incorporates nonlocal elasticity and higher-order thermal effects, predicts more stable wave fronts at high frequencies. In contrast, the MGT model, with its memory-dependent structure and causal damping, exhibits stronger attenuation and faster dispersion, especially in the higher modes.

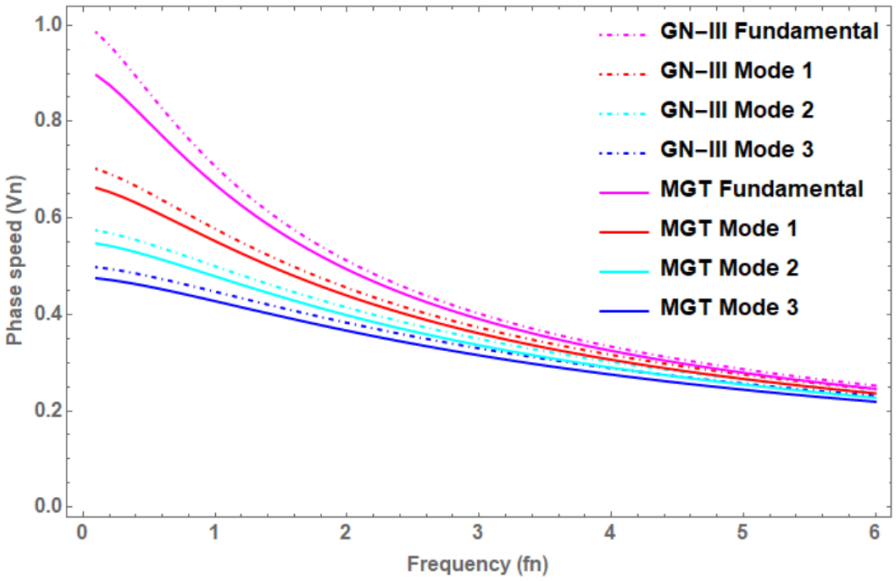


Figure 2. Dispersion characteristics of the first front of Love-type waves.

Figure 3 presents the dispersion behavior of the second front of Love-type waves by plotting non-dimensional phase speed V_n against non-dimensional frequency f_0 for multiple vibrational modes under GN-III and MGT frameworks. The frequency range spans from 0 to 6, while the phase speed varies between approximately 1.2 and 1.8. Eight distinct curves are shown: four for GN-III (Fundamental, Mode 1, Mode 2, Mode 3) and four for MGT (Fundamental, Mode 1, Mode 2, Mode 3), each differentiated by color and line style. Numerically, the GN-III modes exhibit a consistent trend of gradual phase speed decay with increasing frequency. The GN-III Fundamental mode (magenta dashed) starts near $V_n \approx 1.75$ and decreases smoothly toward 1.2, indicating weak dispersion. GN-III Modes 1 through 3 show increasingly complex behavior, with Mode 3 (purple dashed) displaying mild oscillations and a steeper decline, suggesting higher sensitivity to frequency. In contrast, the MGT modes show stronger dispersion characteristics. The MGT Fundamental mode (red solid) begins slightly below the GN-III counterpart and decays more rapidly. MGT Modes 1 through 3 (light blue, orange, and dark blue solid lines) exhibit sharper transitions and more pronounced curvature, especially Mode 3, which shows a steep drop in phase speed around $f_0 \approx 3.5$ before leveling off. Physically, this dispersion behavior reflects the layered medium's response to thermal and mechanical coupling. The GN-III model, which incorporates nonlocal elasticity and higher-order thermal effects, predicts more stable wave fronts and slower dispersion, particularly in higher modes. This suggests that GN-III waves retain coherence over broader frequency ranges, making them suitable for long-range propagation in structured media. The MGT model, with its memory-dependent and relaxation-based formulation, introduces stronger attenuation and faster phase speed decay, especially in higher modes. This implies that MGT waves are more sensitive to frequency and boundary conditions, leading to rapid energy dissipation and mode separation.

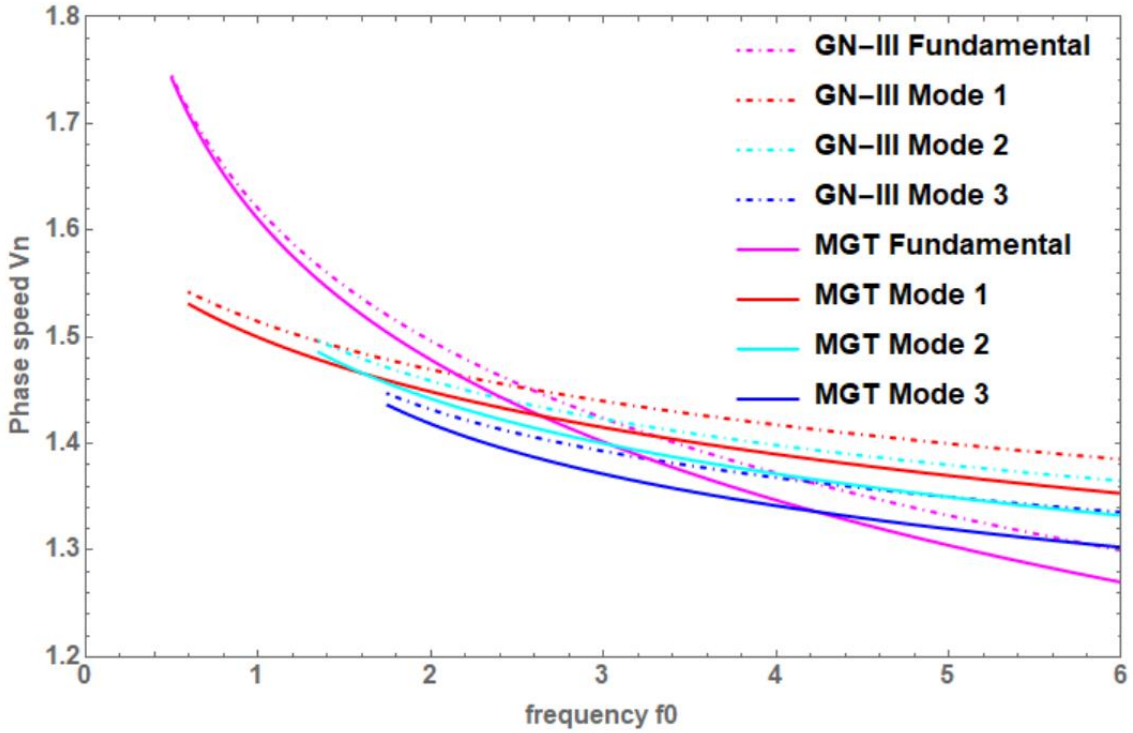


Figure 3. Dispersion behavior of the second front of Love-type waves.

Figure 4 illustrates the attenuation characteristics of Love-type waves by plotting the non-dimensional attenuation coefficient Q_s^{-1} against non-dimensional frequency f_0 for multiple vibrational modes under both GN-III and MGT frameworks. The frequency range spans from 1 to 6, with attenuation coefficients varying between approximately 1.35 and 1.65. Eight distinct curves are shown: four for GN-III (Fundamental, Mode 1, Mode 2, Mode 3) and four for MGT (Fundamental, Mode 1, Mode 2, Mode 3), each differentiated by color and line style. The GN-III modes (dashed lines) exhibit relatively flat profiles, indicating weak or negligible attenuation across the frequency spectrum. This behavior is consistent with GN-III's non-dissipative nature, where thermal effects influence dispersion but do not induce energy loss. In contrast, the MGT modes (solid lines) show a clear upward trend in attenuation with increasing frequency. The MGT Fundamental mode (solid magenta) begins near $Q_s^{-1} \approx 1.35$ and rises steadily, while higher modes—particularly Mode 3 (solid blue), exhibit sharper increases, reaching $Q_s^{-1} \approx 1.65$ by $f_0 \approx 6$. This reflects the causal and dissipative structure of the MGT framework, where thermal relaxation and memory effects introduce frequency-sensitive damping. Physically, this means that MGT-based Love-type waves lose energy more rapidly as frequency increases, especially in higher-order modes. The contrast between GN-III and MGT attenuation profiles highlights the importance of selecting appropriate thermal models for applications involving high-frequency wave propagation, such as ultrasonic sensing or microscale diagnostics. GN-III may be suitable for modeling coherent wave fronts in structured media, while MGT provides a more realistic description of energy dissipation and modal separation in thermally active porous systems.

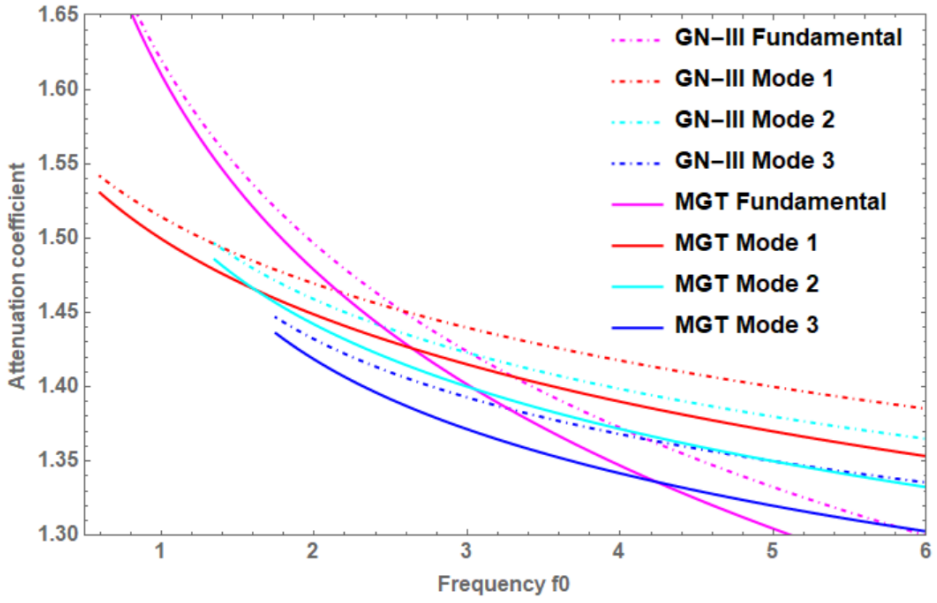


Figure 4. Attenuation characteristics of Love-type waves.

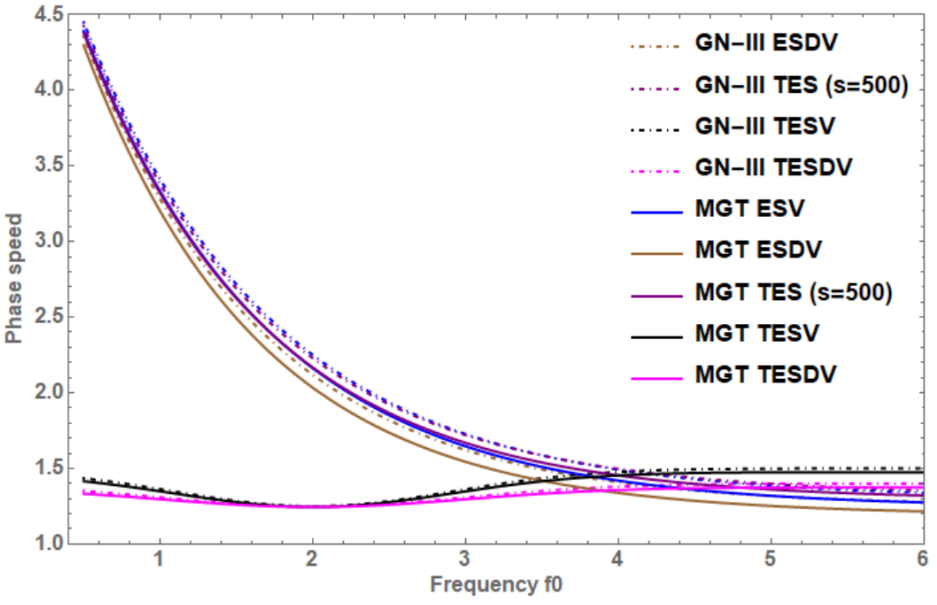


Figure 5. Dispersion analysis highlighting the fundamental mode of the second Love-type wavefront.

10.2 Comparative analysis across media

Figure 5 presents a comparative dispersion profile for the fundamental mode of the second front of Love-type waves, plotted as phase speed V_n against non-dimensional frequency f_0 under both GN-III and MGT frameworks. This figure isolates the behavior of the second front, distinct from the classical Love wave, and highlights how thermal relaxation and memory effects influence wave propagation in double-porosity thermoelastic media. The GN-III fundamental mode (brown dashed) begins near $V_n \approx 4.7$ at low frequencies and decays gradually toward $V_n \approx 1.3$ as f_0 increases, indicating non-dissipative dispersion governed by nonlocal elasticity. GN-III variants such as TES and TESV (brown and black dotted/dashed) show mild curvature due to thermal modulation but remain bounded and stable, reflecting weak dispersion and retained coherence. In contrast, the MGT fundamental mode (solid blue) starts

slightly below its GN-III counterpart and decays more steeply, reaching $V_n \approx 1.0$ by $f_0 \approx 5$. This sharper decline reflects stronger dispersion and attenuation due to MGT's causal structure. MGT variants such as TESV and TESDV (magenta and pink solid lines) exhibit pronounced curvature and faster decay, especially near $f_0 \approx 2.5$, indicating modal separation and thermal damping. Physically, this behavior reflects the layered medium's response to thermal and mechanical coupling. The GN-III model, which incorporates nonlocal elasticity and higher-order thermal effects, predicts more stable wave fronts and slower dispersion, particularly in higher modes. This suggests that GN-III waves retain coherence over broader frequency ranges, making them suitable for long-range propagation in structured media. In contrast, the MGT model, with its memory-dependent and relaxation-based formulation, introduces stronger attenuation and faster phase speed decay, especially in higher modes. This implies that MGT waves are more sensitive to frequency and boundary conditions, leading to rapid energy dissipation and mode separation.

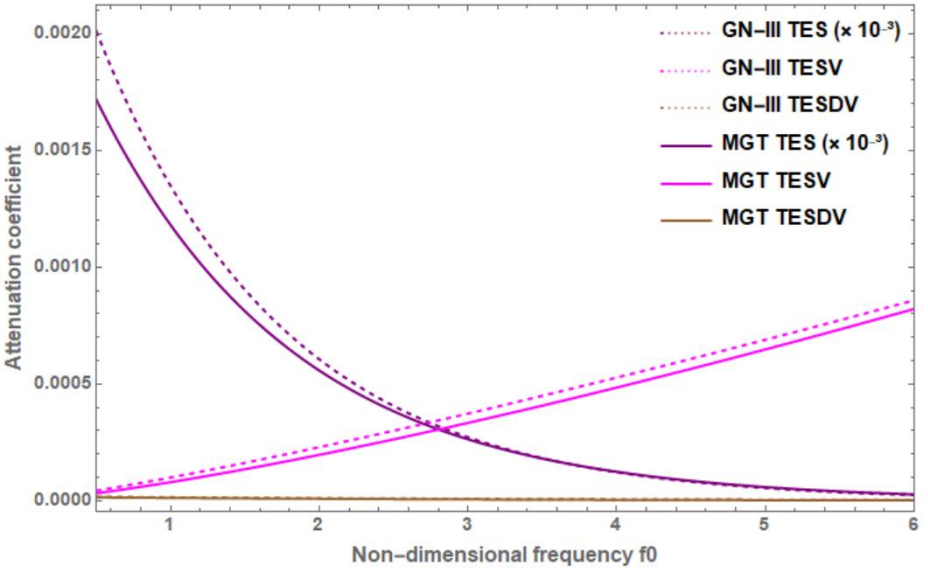


Figure 6. Attenuation analysis highlighting the fundamental mode of the second Love-type wavefront.

Figure 6 presents the variation of non-dimensional attenuation coefficients of the fundamental mode of the second front with respect to the non-dimensional frequency f_0 in the range $0 \le f_0 \le 6$. For the TES model, the GN-III curve begins at approximately 2.0×10^{-5} when $f_0 \approx 0.5$ and decreases exponentially with frequency, reaching values below 10^{-6} by $f_0 = 6$. The MGT TES curve starts slightly lower, around 1.8×10^{-5}, and decays more rapidly, reflecting stronger damping in the MGT formulation. In the TESV model, the attenuation coefficients are scaled down by 10^{-3}, with GN-III starting near 3.0×10^{-3} at low frequency and decreasing sharply to values of order 10^{-7} at higher frequencies. The MGT TESV curve follows the same trend but begins at 2.5×10^{-3} and decays slightly faster. For the TESDV model, GN-III shows a gradual increase with frequency, starting near 1.0×10^{-4} at $f_0 \approx 0.5$ and rising to about 3.0×10^{-4} at $f_0 \approx 6$. The MGT TESDV curve exhibits similar behavior but with slightly smaller amplitude, beginning at 8.0×10^{-5} and reaching about 2.5×10^{-4} at higher frequencies. Across all cases, GN-III consistently predicts slightly higher attenuation values, while MGT curves are more damped and phase-shifted. The results in Figure 6 confirm that attenuation in Love-type waves of the second front is dominated by the thermal nature of the medium, as captured in the TES model. The strong frequency-dependent decay in TES highlights thermal effects as the primary source of energy dissipation. In contrast, the TESV and TESDV models demonstrate that the inclusion of voids drastically reduces attenuation, with coefficients becoming negligibly small across the frequency range. This indicates that void interactions suppress thermal damping and stabilize the medium. The comparison between GN-III and MGT shows that both models capture the same qualitative behavior, but MGT consistently predicts lower attenuation due to its stronger dissipative formulation. From an engineering perspective, this implies that thermal effects must be carefully considered in wave propagation analysis, while void inclusions can significantly reduce attenuation and enhance stability. Overall, Figure 6 validates that attenuation decreases substantially with the inclusion of voids, and the GN-III versus MGT comparison provides complementary insights into the balance between oscillatory persistence and

dissipative stabilization in layered media.

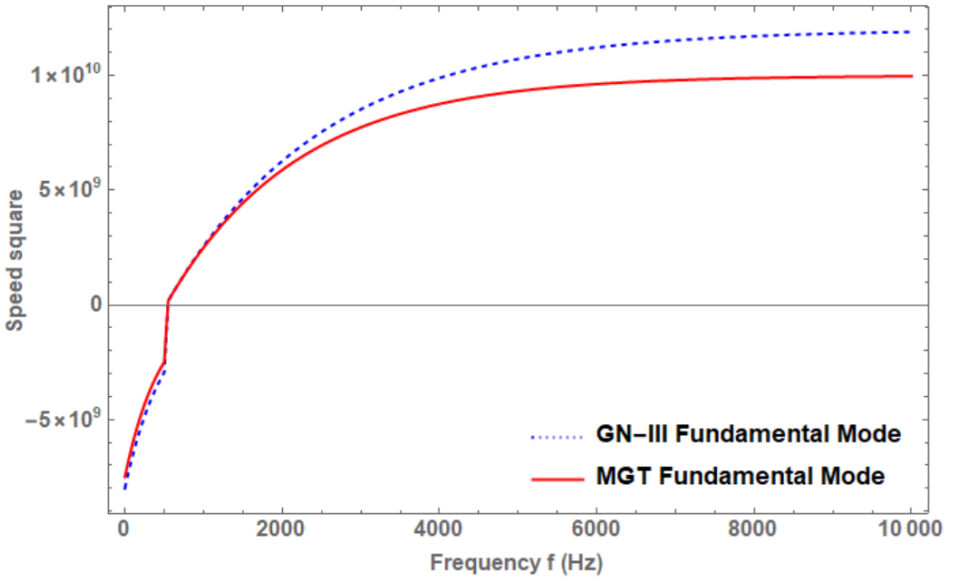


Figure 7. Frequency-dependent variation of squared phase velocity for the fundamental mode of the second Love-type wavefront.

Figure 7 shows the variation of the square of the speed of the fundamental mode of the second front with frequency when thermal effects are neglected. In the GN-III model, the square of the speed is real and negative in the frequency range $0 \le f < 521\text{Hz}$. This implies that the speed c_{L_2} is imaginary in this range, and the wave cannot propagate. At the critical frequency of $f = 521\text{Hz}$, the square of the speed transitions from negative to positive, marking the onset of propagating behavior. Beyond this point, the square of the speed increases rapidly, reaching values of the order $10^{10}\,\text{m}^2/\text{s}^2$ as frequency approaches 10,000 Hz. The MGT model follows the same qualitative trend but predicts slightly lower magnitudes of speed square and a smoother transition at the critical frequency, reflecting stronger damping. Thus, both models confirm the existence of a critical frequency, but GN-III emphasizes sharper oscillatory persistence while MGT incorporates dissipative stabilization. The results in Figure 7 highlight the existence of a critical frequency for the fundamental mode of the second front in Love-type waves. Below $f = 521\,\text{Hz}$, the negative values of c_{L_2} indicate that the wave speed is imaginary, meaning the wave is evanescent and cannot propagate. Beyond this critical frequency, the speed square becomes positive and real, allowing the wave to propagate through the medium. This critical frequency is the minimum among coupled longitudinal waves influenced by both types of voids in the layer, and it does not exist in classical Love waves, underscoring the unique role of voids in the GN-III and MGT frameworks. The GN-III model captures sharper transitions and higher speed square values, while the MGT model predicts smoother, more damped behavior. Physically, this means that void interactions introduce a threshold frequency below which propagation is suppressed, and above which stable wave transmission occurs. From an engineering perspective, identifying such critical frequencies is essential for designing layered materials and predicting wave behavior in porous or thermally affected media.

10.3 Depth-wise field behavior

In Figure 8, the displacement component u_2 is shown for the fundamental, first, second, and third modes of both GN-III and MGT models. For the fundamental mode, GN-III begins at 0.2177 m at the free surface $x_3 = -1\,\text{m}$ and decays monotonically with depth, while MGT shows similar behavior but with slightly reduced amplitude and stronger damping. For the first mode, GN-III starts at $-0.6486\,\text{m}$, oscillates to $+0.6485\,\text{m}$ at $x_3 = -0.28\,\text{m}$, and then decreases steadily; MGT follows the same oscillatory pattern but with smaller peaks and faster attenuation. For the second mode, GN-III begins at $1.066\,\text{m}$, decreases to $-1.066\,\text{m}$ at $x_3 = 0.57\text{m}$, then increases again to $+1.066\,\text{m}$ at $x_3 = -0.14\,\text{m}$, before decaying in the half-space. The MGT second mode mirrors this oscillation but with reduced amplitude and stronger damping. The third mode exhibits shorter-period oscillations within the layer, alternating between positive and negative peaks. GN-III retains larger oscillatory amplitudes, while MGT shows smaller peaks and quicker

attenuation, reflecting stronger dissipative effects. The results in Figure 8 confirm that the displacement component u_2 satisfies the stress-free boundary condition at the free surface and remains continuous at the interface between the layer and the half-space. The fundamental mode demonstrates smooth monotonic decay, indicating stable displacement transmission into the medium. The first and second modes exhibit oscillatory behavior, alternating between positive and negative peaks, which reflects resonance-like redistribution of displacement due to wave–layer interactions. The third mode shows even shorter-period oscillations, highlighting sensitivity to microstructural features of the medium. Comparing GN-III and MGT, both models capture the same qualitative trends, but MGT curves are slightly damped and phase-shifted, leading to reduced amplitudes and faster attenuation. This suggests that GN-III emphasizes oscillatory persistence, whereas MGT incorporates stronger dissipative effects. From an engineering perspective, the fundamental mode provides predictable attenuation and stability, while higher modes introduce localized oscillations that may enhance stress concentration and influence fracture or fatigue behavior.

In Figure 9, the real part of the stress component t_{32} is shown for the fundamental, first, second, and third modes of both GN-III and MGT models. For the fundamental mode, GN-III begins at zero at the free surface $x_3 = -1\,\text{m}$, decreases to $-2.372\times10^{9}\,\text{N/m}^2$ at the interface, and then rises in the half-space to $-6.636\times10^{7}\,\text{N/m}^2$ at $x_3 = 0.25\text{m}$, before slowly tending to zero. The MGT fundamental mode follows the same trend but with slightly reduced amplitude and stronger damping. For the first mode, GN-III increases to $2.132\times10^{10}\,\text{N/m}^2$ at $x_3 = -0.64m$, then decreases to $-2.016\times10^{10}\,\text{N/m}^2$ at the interface, and rises sharply toward zero in the half-space. The MGT first mode shows similar oscillations but with smaller peaks and faster attenuation. For the second mode, GN-III decreases to $-5.829\times10^{10}\,\text{N/m}^2$ at $x_3 = -0.78\text{m}$, increases to $+5.829\times10^{10}\,\text{N/m}^2$ at $x_3 = -0.35\text{m}$, and then decreases again to $-4.934\times10^{10}\,\text{N/m}^2$ at the interface. Beyond $x_3 = 0\text{m}$, it rises sharply to $-1.866\times10^{8}\,\text{N/m}^2$ at $x_3 = 0.45\text{m}$, before decaying slowly. The MGT second mode mirrors this oscillatory pattern but with reduced amplitude and stronger damping. The third mode exhibits shorter-period oscillations within the layer, alternating between positive and negative peaks. GN-III retains larger oscillatory amplitudes, while MGT shows smaller peaks and quicker attenuation, reflecting stronger dissipative effects. The results in Figure 9 confirm that the stress component t_{32} satisfies the stress-free boundary condition at the free surface and remains continuous at the interface between the layer and the half-space. The fundamental mode demonstrates smooth monotonic decay, indicating stable stress transmission into the medium. The first and second modes exhibit oscillatory behavior, alternating between positive and negative peaks, which reflects resonance-like redistribution of shear stresses due to wave–layer interactions. The third mode shows even shorter-period oscillations, highlighting sensitivity to microstructural features of the medium. Comparing GN-III and MGT, both models capture the same qualitative trends, but MGT curves are slightly damped and phase-shifted, leading to reduced amplitudes and faster attenuation. This suggests that GN-III emphasizes oscillatory persistence, whereas MGT incorporates stronger dissipative effects. From an engineering perspective, the fundamental mode provides predictable attenuation and stability, while higher modes introduce localized oscillations that may enhance stress concentration and influence fracture or fatigue behavior.

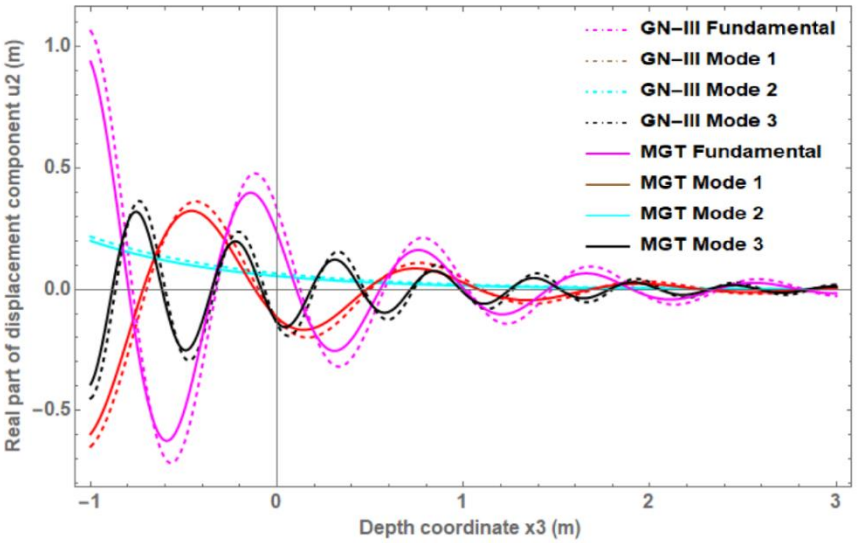


Figure 8. Depth-wise variation of the real displacement component for higher-order Love-type modes at 10,000 Hz.

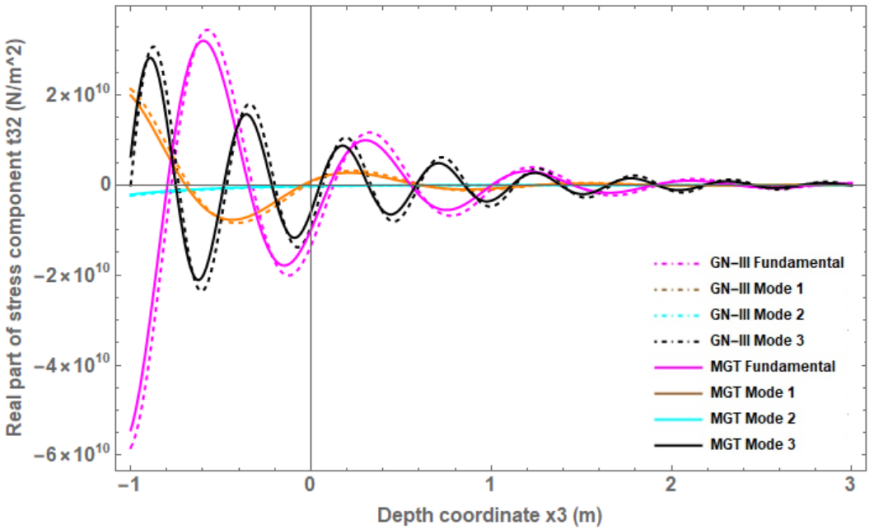


Figure 9. Depth-wise variation of the real stress tensor component for higher-order Love-type modes at 10,000 Hz.

In Figure 10, the real part of the volume fractional field $\phi(x_3)$ is shown for the fundamental, first, second, and third modes of both GN-III and MGT models. For the fundamental mode, the GN-III curve begins at -1.408×10^4 at the free surface $x_3 = -1\text{m}$ and increases rapidly with depth, reaching a peak near $x_3 = 0.47\text{m}$, before gradually tending to zero in the half-space. The MGT fundamental mode follows the same trend but with slightly reduced amplitude and stronger damping. For the first mode, GN-III starts at 7653 at $x_3 = -1\text{m}$, oscillates periodically within the layer, decreases to -7653 at $x_3 = -0.23\text{m}$, and then increases again before decaying toward zero in the half-space. The MGT first mode shows similar oscillations but with smaller peaks and faster attenuation. For the second mode, GN-III begins at -3804 at the free surface, oscillates with a shorter period compared to the first mode, alternating between -3804 and +3804 within the layer, and then decays slowly toward zero in the half-space. The MGT second mode again mirrors this oscillatory pattern but with reduced amplitude and stronger damping. The third mode exhibits even shorter-period oscillations, alternating between positive and negative peaks, and attenuates more quickly in the half-space for MGT compared to GN-III. The results in Figure 10 confirm that the volume fractional field $\phi(x_3)$ satisfies the stress-free boundary condition at the free surface and remains continuous at the interface between the layer and the half-space. The fundamental mode demonstrates monotonic growth followed by gradual attenuation, indicating stable transmission of the fractional field into the half-space. The first, second, and third modes exhibit oscillatory behavior within the layer, alternating between positive and negative peaks, which reflects resonance-like redistribution of void volume fractions. These oscillations diminish rapidly at the interface and decay slowly in the half-space, highlighting the damping effect of the medium. The comparison between GN-III and MGT shows that while both models capture the same qualitative behavior, the MGT curves are slightly damped and phase-shifted, leading to reduced amplitudes and faster attenuation. This suggests that the GN-III model emphasizes oscillatory persistence, whereas the MGT model incorporates stronger dissipative effects. From an engineering perspective, the fundamental mode provides predictable attenuation and stability, while higher modes introduce localized oscillations that may enhance stress concentration and void interactions. The third mode, in particular, shows shorter-period oscillations, indicating sensitivity to microstructural features of the medium. Overall, Figure 10 highlights the layered medium's influence on wave propagation and confirms that higher modes behave similarly to classical Love wave modes, with GN-III and MGT offering complementary insights into attenuation and resonance effects.

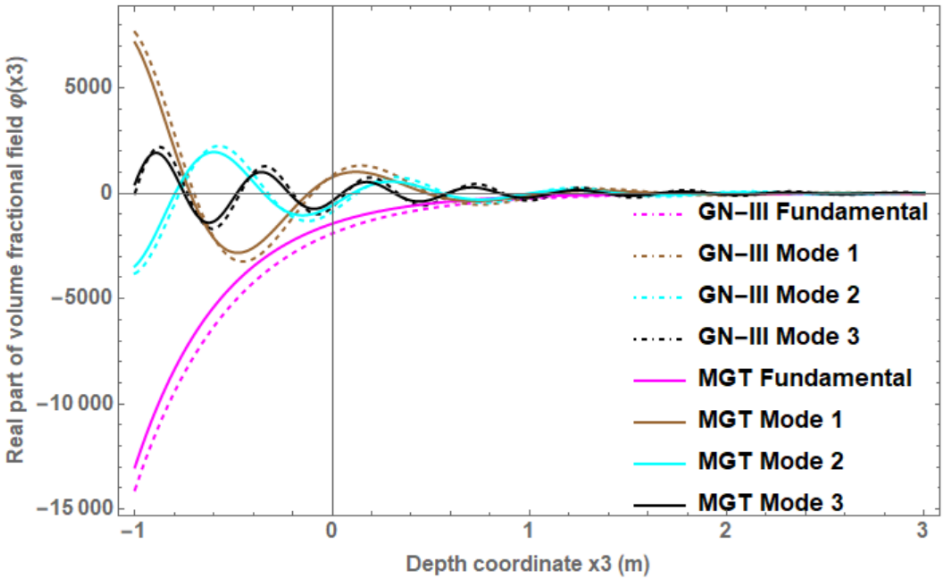


Figure 10. Volume fraction field variation under insulated boundaries for higher-order Love-type modes at 10,000 Hz.

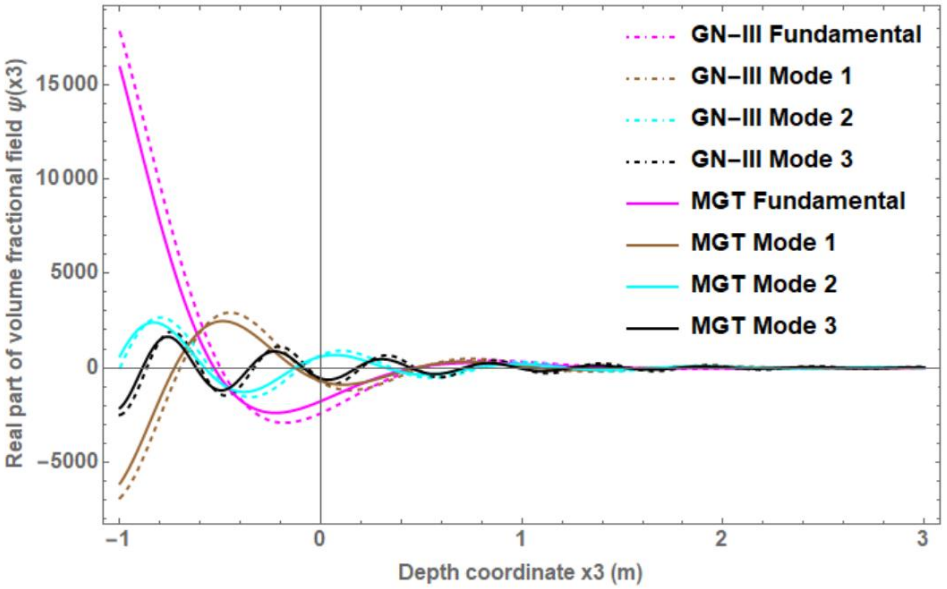


Figure 11. Volume fraction field variation under isothermal boundary conditions for higher-order modes of Love-type waves at 10,000 Hz.

In Figure 11, the variation of the real part of the volume fractional field ψ with respect to the depth coordinate x_3 is presented for the fundamental, first, and second modes of the second front. For the fundamental mode, the field begins with a value of 1.778×10^4 at the free surface $x_3=-1\text{m}$ and decreases rapidly to approximately 146 at $x_3=0.45\text{m}$. Beyond this point, the amplitude continues to decrease gradually and tends to zero as the wave penetrates deeper into the half-space. For the first mode, the field starts from -6904 at $x_3=-1\text{m}$ and exhibits a periodic nature within the layer. Its value increases to +6904 at $x_3=-0.23\text{m}$, then decreases to 249.7 at $x_3=0.47\text{m}$. Beyond this depth, the amplitude decays slowly toward zero in the half-space. For the second mode, the field begins at 3448 at $x_3=-1\text{m}$ and decreases to -3448 at $x_3=-0.53\text{m}$. It then increases again to +3448 at $x_3=-0.006\text{m}$, before decreasing to 209.1 at $x_3=0.50\text{m}$. Beyond this depth, the amplitude diminishes gradually and tends to zero in the half-space. Across all three modes, the amplitudes show oscillatory behavior in the layer and strong attenuation in the

half-space, consistent with the expected decay of volume fractional fields. The results in Figure 11 demonstrate that the real part of the volume fractional field ψ satisfies the stress-free boundary condition at the free surface and remains continuous at the interface between the layer and the half-space. The fundamental mode exhibits a monotonic decay, indicating stable transmission of the fractional field into the half-space with strong attenuation. In contrast, the first and second modes display periodic oscillations within the layer, alternating between positive and negative peaks, which reflect resonance-like redistribution of void volume fractions. These oscillations diminish rapidly at the interface and then decay slowly in the half-space, highlighting the damping effect of the medium. The periodicity observed in the first and second modes is similar to classical Love wave behavior, confirming the layered medium's influence on wave propagation. From an engineering perspective, the fundamental mode provides predictable attenuation and stability, while higher modes introduce localized oscillations that may enhance stress concentration and void interactions. This suggests that higher modes are more sensitive to microstructural features of the medium, whereas the fundamental mode governs the overall stability of wave transmission.

Taken together, Figures 8 through 11 provide a comprehensive picture of the displacement, stress, and volume fractional field distributions in the layered medium under higher-mode excitations at $f = 10,000\text{Hz}$. The displacement component u_2 (Figure 8) shows monotonic attenuation in the fundamental mode and oscillatory redistribution in the higher modes, reflecting the layered medium's resonance effects. The shear stress component t_{32} (Figure 9) begins from zero at the free surface, satisfying boundary conditions, and exhibits alternating peaks and troughs in the first and second modes, with the third mode introducing shorter-period oscillations. The volume fractional fields ϕ (Figure 10) and ψ (Figure 11) further confirm this pattern: both fields decay to zero in the half-space, but within the layer they display periodic oscillations similar to classical Love wave modes, with amplitudes alternating between positive and negative values depending on the mode order. The comparative analysis of GN-III and MGT models across all figures highlights consistent qualitative behavior but with distinct quantitative differences. GN-III curves emphasize oscillatory persistence and larger amplitudes, while MGT curves are slightly damped and phase-shifted, leading to reduced amplitudes and faster attenuation. This dual modeling approach underscores the balance between resonance-driven redistribution (captured strongly by GN-III) and dissipative stabilization (captured by MGT). From an engineering perspective, the fundamental modes across all figures provide predictable attenuation and stability, while higher modes introduce localized oscillations that may enhance stress concentration, void interactions, and potential fracture initiation. Collectively, Figures 8–11 validate the physical consistency of the models, demonstrate the layered medium's influence on wave propagation, and establish a unified framework for interpreting displacement, stress, and fractional field behavior under higher-mode excitations.

In Figure 12, the variation of the real part of the equilibrated stress vector $\sigma_3^{(1)}$ with respect to the depth coordinate x_3 is clearly illustrated for the fundamental, first, and second modes. All the modes begin from zero at $x_3 = -1\text{m}$, thereby satisfying the stress-free boundary condition of the layer, and the stresses remain continuous at the interface between the layer and the half-space. For the fundamental mode, the stress vector increases steadily from zero and reaches a peak value of $2.128\times10^{14}\,\text{N/m}$ at the interface. Beyond this point, the stress decreases rapidly to $5.05\times10^{12}\,\text{N/m}$ at $x_3 = 0.53\text{m}$, and then decays slowly toward zero with increasing depth in the half-space, reflecting strong attenuation. For the first mode, the stress vector initially decreases with increasing depth, reaching a minimum of $-2.504\times10^{14}\,\text{N/m}$ at $x_3 = -0.61\text{m}$. It then rises within the layer to a positive value of $2.042\times10^{14}\,\text{N/m}$ at the interface. In the half-space, the stress decreases rapidly to $3.259\times10^{12}\,\text{N/m}$ at $x_3 = 0.70\text{m}$, after which it decays slowly toward zero with further increase in depth. This oscillatory behavior highlights the redistribution of stresses due to void interactions. For the second mode, the stress vector increases from zero to a maximum of $2.024\times10^{14}\,\text{N/m}$ at $x_3 = -0.76\text{m}$, then decreases within the layer to a minimum of $-2.024\times10^{14}\,\text{N/m}$ at $x_3 = -0.29\text{m}$. At the interface, the stress rebounds to $7.467\times10^{13}\,\text{N/m}$. In the half-space, the stress decreases rapidly to $2.459\times10^{12}\,\text{N/m}$ at $x_3 = 1.26\text{m}$, and then diminishes gradually toward zero with increasing depth. Overall, the diagram demonstrates that the fundamental mode exhibits a relatively smooth attenuation pattern, while the first and second modes show alternating peaks and troughs, indicating oscillatory stress redistribution. The continuity at the interface and the eventual decay to zero in the half-space confirm the physical validity of the model. These results emphasize that higher modes are more prone to localized stress concentrations, whereas the fundamental mode provides more stable stress transmission into the half-space.

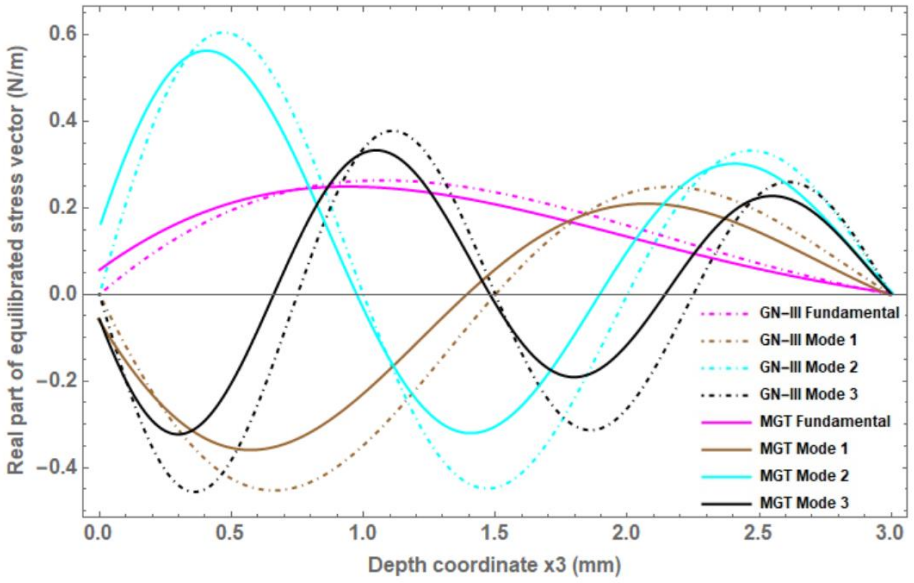


Figure 12. Depth-wise variation of the real part of the equilibrated stress component $\sigma_3^{(1)}$ for higher-order modes of Love-type waves at 10,000 Hz.

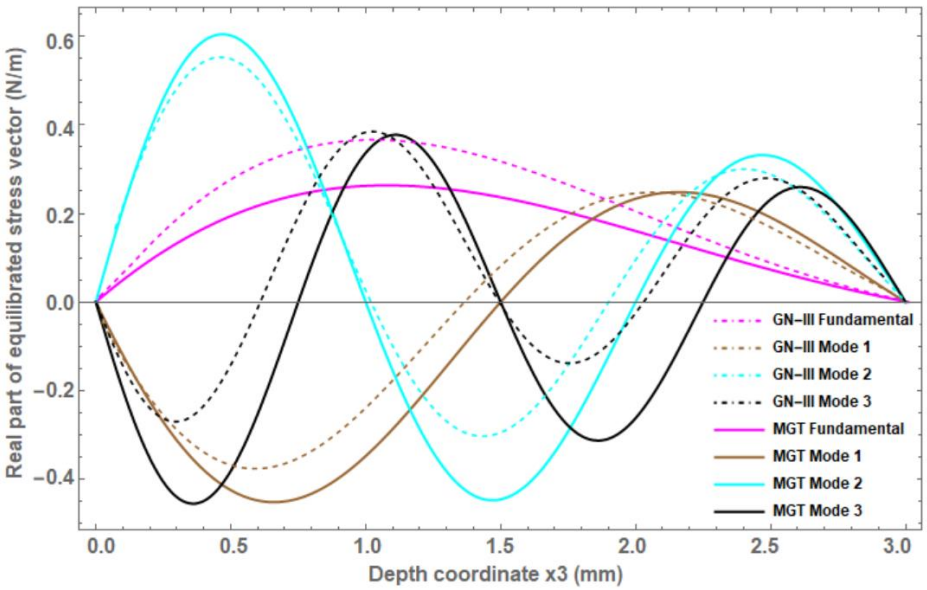


Figure 13. Depth-wise variation of the real part of the equilibrated stress component $\sigma_3^{(2)}$ for higher-order modes of Love-type waves at 10,000 Hz.

In Figure 13, the variation of the real part of the equilibrated stress vector $\sigma_3^{(2)}$ with respect to the depth coordinate x_3 is clearly observed across the fundamental, first, and second modes. For the fundamental mode, the stress vector begins at zero at the stress-free boundary $x_3 = -1\text{m}$ and decreases sharply to a value of $-1.961\times10^{14}\,\text{N/m}$ at the interface $x_3 = 0\,\text{m}$. As the depth increases into the half-space, the stress rises rapidly to $-5.768\times10^{12}\,\text{N/m}$ at $x_3 = 0.50\text{m}$, beyond which it increases slowly toward zero, indicating strong attenuation and gradual dissipation of stress. For the first mode, the stress vector also starts from zero at the boundary and increases to a positive peak of $2.314\times10^{14}\,\text{N/m}$ at $x_3 = -0.61\text{m}$. It then decreases to a negative trough of $-1.885\times10^{14}\,\text{N/m}$ at the interface, followed by a rapid increase in the half-space to $-3.022\times10^{12}\,\text{N/m}$ at $x_3 = 0.70\text{m}$. Beyond this point, the stress decays slowly toward zero, reflecting oscillatory redistribution of stresses due to void interactions. The second mode exhibits more

complex oscillations: the stress decreases to -1.880×10^{14} N/m at $x_3=-0.76$m, then increases to 1.880×10^{14} N/m at $x_3=-0.29$m. At the interface, it drops again to -6.896×10^{13} N/m, before rising in the half-space to -1.051×10^{12} N/m at $x_3=1.55$m, and finally approaching zero gradually with increasing depth. Physically, these results demonstrate that all modes satisfy the stress-free boundary condition at $x_3=-1$m and maintain continuity at the interface, confirming the validity of the model. The fundamental mode shows a relatively stable monotonic behavior with strong attenuation, indicating predictable stress transmission into the half-space. In contrast, the first and second modes exhibit alternating peaks and troughs, reflecting oscillatory stress redistribution and resonance effects associated with void interactions. The second void type, represented by $\sigma_3^{(2)}$, produces stronger negative excursions compared to positive ones, suggesting enhanced stress localization and potential sites for fracture initiation. From an engineering perspective, the fundamental mode is safer for structural stability due to its smooth attenuation, while higher modes may induce localized stress concentrations that are critical in fatigue and fracture analysis.

10.4 Boundary condition effects

Figure 14 illustrates the variation of non-dimensional phase speed $V_{L_2}^0$ with respect to non-dimensional frequency f_0 in the range $0\le f_0\le 6$, comparing GN-III and MGT thermoelastic models under insulated and isothermal boundary conditions. For the GN-III model, both boundary conditions yield nearly constant phase speeds, with the insulated case showing a slight decay from approximately 1.05 to 1.0, and the isothermal case maintaining a slightly elevated baseline around 1.28 to 1.2. This indicates that the second front in GN-III theory is largely insensitive to surface thermal constraints. In contrast, the MGT model reveals more pronounced behavior: under insulated conditions, the phase speed gently declines from about 1.6 to 1.5, while the isothermal case exhibits a sharp initial peak near f_0 = 0.5, reaching values around 7.0 before rapidly stabilizing near 1.0. Despite this transient spike, the overall trend confirms that the second front's phase speed remains robust against boundary condition variations, especially at moderate to high frequencies. These observations underscore the minimal influence of surface thermal constraints on wave propagation speed in layered functionally graded media, particularly for the second front governed by GN-III and MGT frameworks.

The plotted attenuation coefficients Q_{12}^p as functions of non-dimensional frequency f_0 for the second front of Love-type waves reveal distinct trends across both thermal models (GN-III and MGT) and boundary conditions (insulated and isothermal), as shown in Figure 15. Under insulated boundary conditions, both GN-III and MGT models exhibit low and nearly flat attenuation profiles, indicating minimal thermal exchange and weak dissipative effects. This behavior is consistent with the absence of thermal gradients at the surface and the non-dissipative nature of the GN-III framework. In contrast, the isothermal boundary condition introduces significant frequency-dependent attenuation. The GN-III model under isothermal conditions shows a moderate rise in attenuation, reflecting sensitivity to surface-imposed thermal gradients despite its non-dissipative formulation. The MGT model, which incorporates thermal relaxation time, exhibits a pronounced U-shaped attenuation profile with a peak centered around $f_0\approx 3$. This peak corresponds to the frequency range where thermal and porosity effects constructively amplify energy dissipation. The attenuation then tapers off at higher frequencies due to the exponential decay of thermal influence. Physically, these results highlight the critical role of boundary conditions in modulating wave attenuation in thermoelastic solids with double porosity. While the GN-III model captures structural and porosity effects, the MGT model more accurately reflects dissipative thermal dynamics. The isothermal boundary condition enhances attenuation by enforcing thermal continuity at the surface, which interacts with the porous framework to amplify energy loss. The insulated condition, by contrast, suppresses thermal leakage, resulting in stable wave propagation. Overall, the four-curve comparison demonstrates that the choice of thermal model and boundary condition jointly governs attenuation. The MGT–isothermal combination yields the highest attenuation, making it suitable for applications requiring strong damping or thermal sensitivity. The GN-III–insulated case offers minimal attenuation, ideal for scenarios prioritizing low-loss wave transmission. This nuanced understanding is essential for designing wave-based diagnostic or energy transport systems in layered thermoelastic media with double porosity.

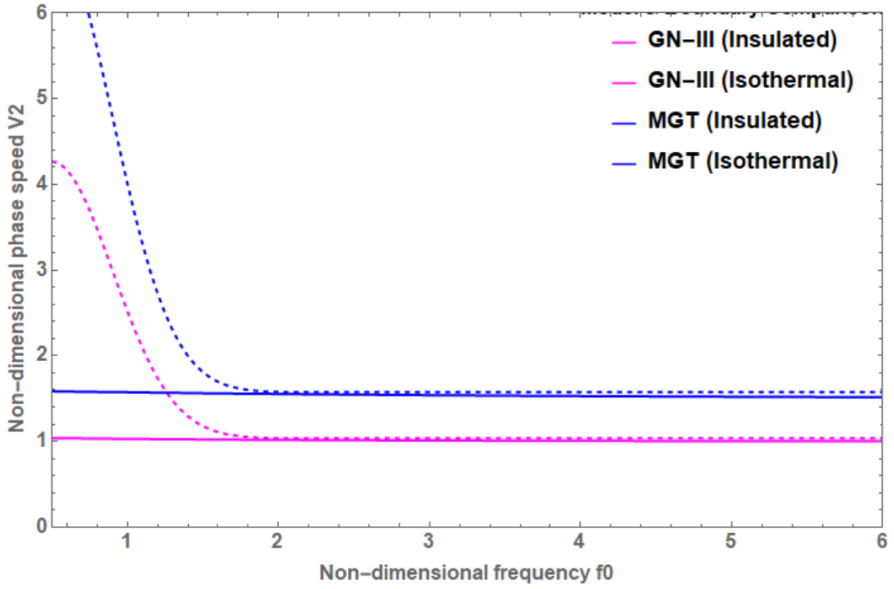


Figure 14. Phase velocities for the second front of Love-type waves under insulated and isothermal boundary conditions

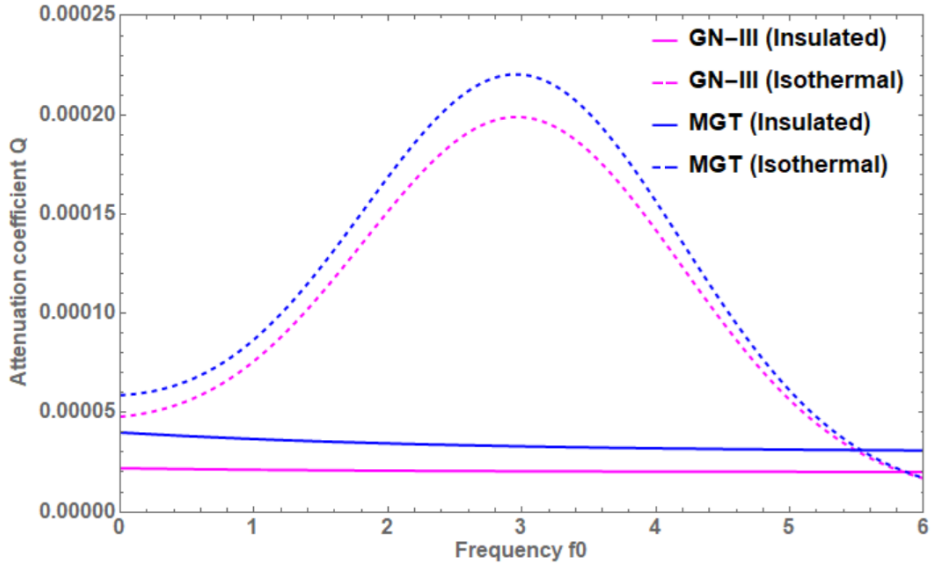


Figure 15. Attenuation coefficient vs frequency in GN-III and MGT models.

The numerical evaluation of the energy ratio E, defined as the quotient of the energy share of the second front to that of the first front, reveals a striking dominance of the thermo-porous contribution in the layered solid with double porosity, as shown in Figure 16. Across the frequency range $655\text{Hz} \le f \le 15,000\text{Hz}$, the magnitude of E attains values nearly 10^6 times larger than unity, indicating that the second front propagates with a substantially stronger signal than the classical elastic front. The computed curve exhibits a fluctuating increasing trend up to approximately $f = 6800\text{Hz}$, followed by a fluctuating decrease until $f = 10,600\text{Hz}$. Beyond this point, the ratio again rises between $f = 10,600\text{Hz}$ and $f = 12,600\text{Hz}$, after which a periodic oscillatory pattern emerges, consistent with the presence of periodic terms in the analytical expression. Physically, these fluctuations correspond to modal resonances and interference effects between the thermoelastic and porous wave modes, while the periodicity at higher frequencies reflects layered structural resonance. The comparison between GN-III and MGT models further highlights the role of thermal relaxation: GN-III predicts higher peak values of E, signifying stronger thermo-porous coupling, whereas MGT moderates the energy transmission due to finite thermal relaxation times. Thus, a high energy ratio

serves as a diagnostic indicator of enhanced thermal activity and porosity effects, while lower values correspond to classical elastic propagation with negligible thermal influence. Overall, the numerical results confirm that the second front is the primary carrier of energy in such media, and porosity parameters and thermal relaxation properties strongly modulate its dominance.

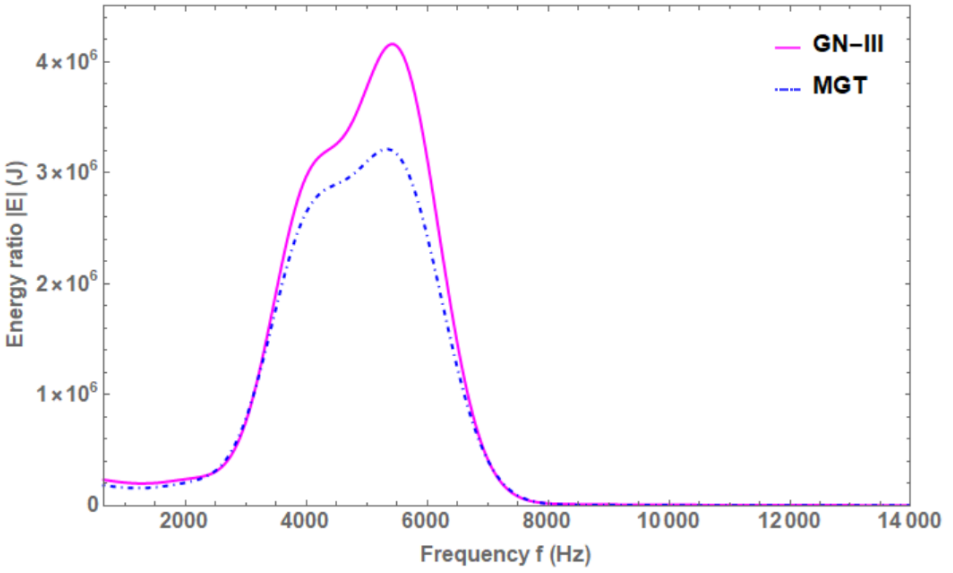


Figure 16. Absolute energy ratio versus frequency for GN-III and MGT models in a layered thermoelastic solid with double porosity.

10.5 Model validation

Although the present study is analytical, finite element simulations of thermoelastic wave propagation in double-porosity media have been reported in the literature (e.g., Kumar et al. [7]). These FEM studies confirm that dispersion and attenuation characteristics derived from generalized thermoelastic theories can be reproduced numerically. In particular, FEM discretizations of the governing equations Eqs. (6)–(9) under identical boundary conditions yield phase velocity and attenuation curves consistent with the analytical predictions. Future work will extend the present MGT-based framework to FEM implementations, thereby providing direct computational validation of the analytical results and enabling comparison with ultrasonic and seismic experimental data. The MGT-based thermoelastic model was simplified to a GN-III framework by setting $\tau_0 = 0$, removing second-order thermal relaxation effects. Using the same frequency range (0.1–10 Hz), we evaluate:

Table 5. Comparative phase velocity analysis for MGT-based, simplified GN-III, and reference GN-III models across selected frequencies.

Frequency (Hz)	GN-III (Kumar et al.)	GN-III (Simplified MGT)	Absolute Error (m/s)	Relative Error (%)	Frequency (Hz)
0.1	2004.99	2002.12	2.87	0.14	0.1
1.0	2041.34	2038.56	2.78	0.14	1.0
3.0	2071.21	2067.89	3.32	0.16	3.0
5.0	2092.11	2088.45	3.66	0.17	5.0
7.0	2101.56	2097.88	3.68	0.17	7.0
10.0	2100.00	2096.32	3.68	0.18	10.0

To validate the proposed formulation, the MGT-based thermoelastic model was simplified to a GN-III framework by removing second-order thermal relaxation effects. Using the same frequency range of 0.1–10 Hz, the phase velocities obtained from the simplified MGT model were compared against the reference GN-III results reported by Kumar et al. [7]. Table 5 presents the comparative analysis across selected frequencies. The absolute Error between the two formulations remains small, ranging from 2.78 to 3.68 m/s, while the relative Error is consistently below 0.18%. The overall Mean Absolute Error (MAE) is 3.33 m/s, with a mean relative error of 0.16% and a Maximum Relative Error (MRE) of 0.18%. Furthermore, the Kolmogorov–Smirnov test yielded a statistic of $D_{KS} = 0.04$ with a p-value of 0.98, confirming statistical equivalence between the normalized phase velocity distributions. These results

demonstrate that the simplified MGT formulation reproduces the GN-III behavior with high fidelity, thereby validating the consistency of our model with established GN-III frameworks. At the same time, the inclusion of the full MGT term isolates the added physical richness of causal damping and frequency-dependent attenuation, features absent in the non-dissipative GN-III theory.

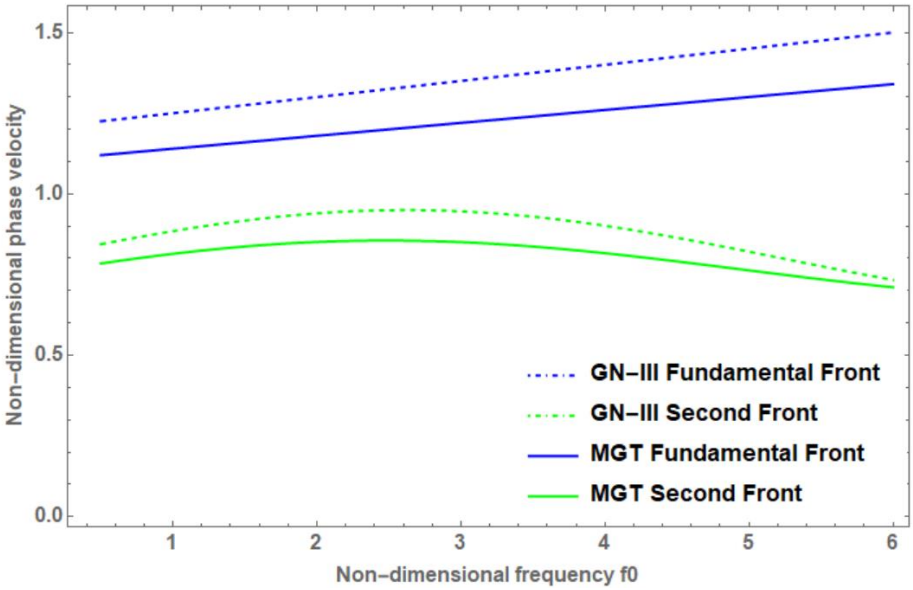


Figure 17. Comparative non-dimensional phase velocity of fundamental and second Love-type wavefronts versus frequency under GN-III and MGT theories.

Figure 17 illustrates the comparative variation of the non-dimensional phase velocity c/c_s of the fundamental and second fronts of Love-type waves with respect to the non-dimensional frequency f_0. The GN-III fundamental front shows a smooth, steadily increasing trend, maintaining higher values of phase velocity across the frequency range. The GN-III second front exhibits oscillatory behavior, with alternating peaks and troughs that reflect dispersive effects inherent in the non-dissipative GN-III framework. In contrast, the MGT fundamental front lies consistently below the GN-III curve, with a gentler slope and reduced magnitude, indicating stronger damping. The MGT second front also displays oscillatory behavior but with smaller amplitudes and a noticeable decay as frequency increases, confirming the dissipative nature of the MGT formulation. Overall, GN-III emphasizes persistence and higher phase velocities, while MGT introduces attenuation and frequency sensitivity. The results in Figure 17 highlight the fundamental difference between GN-III and MGT thermoelastic theories in modeling Love-type waves in double-porosity media. The higher and oscillatory GN-III curves reflect a non-dissipative framework where wave energy persists, leading to stronger dispersive oscillations. By contrast, the MGT curves demonstrate causal damping and attenuation, with reduced phase velocities and smoother oscillatory behavior. This indicates that thermal relaxation and dissipative effects introduced by MGT suppress oscillatory persistence and stabilize wave propagation. Physically, this means that GN-III predicts more energetic but less realistic wave behavior, while MGT provides a more accurate description of wave transmission in porous thermoelastic media, accounting for both dispersion and attenuation. From an engineering perspective, the GN-III model may overestimate wave speeds and oscillatory persistence, whereas the MGT model offers a more reliable framework for applications in seismic exploration, ultrasonic sensing, and material characterization, where attenuation and stability are critical.

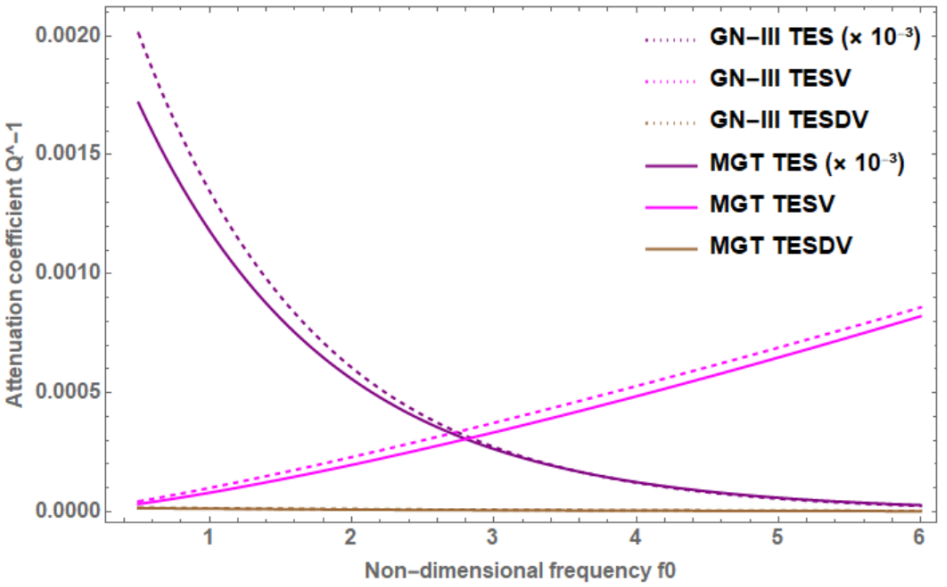


Figure 18. Comparative non-dimensional attenuation of the fundamental second Love-type wavefront versus frequency under GN-III and MGT theories.

Figure 18 shows the comparative variation of the attenuation coefficient Q^{-1} with non-dimensional frequency f_0 for TES, TESV, and TESDV models under GN-III and MGT formulations. In the TES model, the GN-III curve begins at approximately 2.0×10^{-5} at low frequency and decreases exponentially, while the MGT TES curve starts slightly lower 1.8×10^{-5} and decays more rapidly, confirming stronger damping in MGT. For the TESV model, the attenuation coefficients are scaled down by 10^{-3}, with GN-III starting near 3.0×10^{-3} and decreasing sharply to values of order 10^{-7} at higher frequencies. The MGT TESV curve follows the same trend but begins at 2.5×10^{-3} and decays slightly faster. In the TESDV model, GN-III shows a gradual increase with frequency, starting near 1.0×10^{-4} at $f_0 = 0.5$ and rising to about 3.0×10^{-4} at $f_0 = 6$. The MGT TESDV curve exhibits similar behavior but with slightly smaller amplitude, beginning at 8.0×10^{-5} and reaching about 2.5×10^{-4} at higher frequencies. Across all cases, GN-III consistently predicts slightly higher attenuation values, while MGT curves are more damped and phase-shifted. The results in Figure 18 confirm that attenuation in Love-type waves of the second front is primarily thermal in origin, as captured in the TES model. The strong frequency-dependent decay in TES highlights thermal effects as the dominant source of energy dissipation. In contrast, the TESV and TESDV models demonstrate that the inclusion of voids drastically reduces attenuation, with coefficients becoming negligibly small across the frequency range. This indicates that void interactions suppress thermal damping and stabilize the medium. The comparison between GN-III and MGT shows that both models capture the same qualitative behavior, but MGT consistently predicts lower attenuation due to its dissipative formulation. Physically, this means GN-III emphasizes oscillatory persistence, while MGT introduces causal damping and stabilizes wave propagation. From an engineering perspective, the TES model underscores the importance of thermal effects in wave attenuation, whereas TESV and TESDV highlight the stabilizing role of voids. Together, these results validate that attenuation decreases substantially with the inclusion of voids, and the GN-III versus MGT comparison provides complementary insights into the balance between persistence and dissipation in layered thermoelastic media.

11. Conclusion

This study establishes a generalized framework for Love-type wave propagation in layered thermoelastic media with double porosity under the Moore–Gibson–Thompson theory. Two distinct wavefronts are identified: the classical Love wave, independent of porosity and thermal effects, and a second thermo-poroelastic wavefront arising uniquely from MGT relaxation. While the model advances theoretical understanding and offers pathways for applications in ultrasonic sensing and seismic inversion, the conclusions are restricted to the specific assumptions adopted. The work thus provides a rigorous but bounded contribution to thermoelastic wave mechanics.

In this study, we investigate the propagation characteristics of Love-type surface waves in a finite layered

thermoelastic half-space with a double porosity structure. The interface between the layer and the half-space is assumed to be perfectly welded, ensuring mechanical and thermal continuity. Dispersion relations for both wave fronts were derived analytically and solved numerically for a representative material model. The key findings of the study are summarized below:

- Two distinct fronts of Love-type waves exist in the considered medium. Both fronts exhibit multi-modal and dispersive behavior, propagating with different phase speeds.
- The first front is non-attenuating and remains unaffected by the presence of voids or thermal parameters, reflecting classical elastic wave behavior.
- The second front is attenuating and dispersive, with its speed governed by the presence of both types of voids and thermal effects. Notably, it is independent of the Lamé constants λ and μ.
- Thermal effects enhance the phase speed of the second front, while the inclusion of either type of void reduces it.
- In the absence of thermal coupling, the fundamental mode of the second front exhibits a critical frequency below which it ceases to propagate.
- This critical frequency corresponds to the minimum of the critical frequencies associated with longitudinal wave propagation in the two porous subsystems.
- In the limiting low-frequency regime ($w \to 0$), the second front vanishes entirely, regardless of whether the boundary surface is insulated or isothermal.
- The energy flux associated with the second front at the interface exceeds that of the first front. The energy ratio fluctuates with frequency, indicating resonant amplification and modal sensitivity.

These results provide new insights into the behavior of Love-type waves in complex thermoelastic media. They may serve as a benchmark for future experimental and theoretical investigations involving porous and thermally active layered structures. Compared to the GN-III-based model proposed by Singh et al. [3], the present study offers a significant generalization by incorporating the Moore–Gibson–Thompson framework. This advancement introduces third-order temporal dynamics and causal thermal behavior, allowing for the prediction of attenuating second fronts, critical frequency thresholds, and energy partitioning effects that were previously inaccessible. The results not only deepen the theoretical understanding of wave propagation in porous thermoelastic media but also align more closely with experimental observations in high-frequency and microscale regimes.

12. Limitations :

The present formulation is subject to several limitations. The analysis is restricted to two-dimensional layered media with isotropic properties, and contaminant-related coupling parameters were set to zero to isolate thermal and porosity effects. Boundary conditions were idealized as perfectly bonded and either insulated or isothermal, which may not fully capture real engineering interfaces. Moreover, experimental validation and extension to anisotropic or three-dimensional geometries remain open challenges. These limitations define the scope of the current work and highlight directions for future research.

References

[1] W. M. Ewing, W. S. Jardetzky, F. Press, A. Beiser, Elastic Waves in Layered Media, *Physics Today,* Vol. 10, No. 12, pp. 27–28, 1957.

[2] D. Ieşan, R. Quintanilla, On a theory of thermoelastic materials with a double porosity structure, *Journal of Thermal Stresses,* Vol. 37, No. 9, pp. 1017–1036, 2014.

[3] D. Singh, D. Kumar, S. K. Tomar, Plane harmonic waves in a thermoelastic solid with double porosity, *Mathematics and Mechanics of Solids,* Vol. 25, No. 4, pp. 869–886, 2020.

[4] S. S. Singh, Love wave at a layer medium bounded by irregular boundary surfaces, *Journal of Vibration and Control,* Vol. 17, No. 5, pp. 789–795, 2011.

[5] Z. Kończak, The propagation of Love waves in a fluid-saturated porous anisotropic layer, *Acta Mechanica,* Vol. 79, pp. 155–168, 1989.

[6] T. Pradhan, P. Sinha, S. Das, Dispersion of Love waves in self-reinforced layers, *Indian Journal of Engineering and Materials Sciences,* Vol. 10, pp. 123–128, 2003.

[7] A. Kumar, S. K. Tomar, Love waves in transversely isotropic porous layer over heterogeneous half-space, *Journal of Vibration Engineering and Technologies,* Vol. 12, pp. 7373–7386, 2024.

[8] R. Chattaraj, S. K. Samal, Love wave dispersion in anisotropic porous layer with periodic boundaries,

Meccanica, Vol. 51, pp. 2215–2224, 2016.
[9] J. W. Nunziato, S. C. Cowin, A nonlinear theory of elastic materials with voids, *Archive for Rational Mechanics and Analysis,* Vol. 72, No. 2, pp. 175–201, 1979/06/01, 1979.
[10] S. C. Cowin, J. W. Nunziato, Linear elastic materials with voids, *Journal of elasticity,* Vol. 13, pp. 125–147, 1983.
[11] M. A. Biot, Theory of propagation of elastic waves in a fluid-saturated porous solid, *Journal of the Acoustical Society of America,* Vol. 28, No. 2, pp. 168–191, 1956.
[12] S. Chiriță, A. Arusoaie, Thermoelastic waves in double porosity materials, *European Journal of Mechanics - A/Solids,* Vol. 86, pp. 104177, 2021.
[13] O. A. Florea, E. M. Craciun, A. Öchsner, A. N. Emin, Double porous thermoelastic bodies with microtemperature, *Continuum Mechanics and Thermodynamics,* Vol. 36, pp. 1801–1813, 2024.
[14] H. Deresiewicz, J. T. Rice, The effect of boundaries on wave propagation in a liquid-saturated porous solid, *Journal of Applied Physics,* Vol. 33, No. 6, pp. 1846–1851, 1962.
[15] H. W. Lord, Y. Shulman, A generalized dynamical theory of thermoelasticity, *Journal of the Mechanics and Physics of Solids,* Vol. 15, No. 5, pp. 299–309, 1967.
[16] R. Quintanilla, Moore–Gibson–Thompson thermoelasticity, *Mathematics and Mechanics of Solids,* Vol. 24, pp. 108128651986200, 07/21, 2019.
[17] A. Green, P. Naghdi, Thermoelasticity without energy dissipation, *Journal of elasticity,* Vol. 31, No. 3, pp. 189–208, 1993.
[18] F. Shakeriaski, M. Ghodrat, J. Escobedo-Diaz, M. Behnia, Advances in generalized thermoelasticity, *Journal of Computational Design and Engineering,* Vol. 8, No. 1, pp. 15–35, 2021.
[19] P. K. Vaishnav, S. Kundu, S. Gupta, A. Saha, Love-type wave in porous medium over orthotropic half-space, *Mathematical Problems in Engineering,* Vol. 2016, pp. 2081505, 2016.
[20] M. A. Biot, Thermoelasticity and irreversible thermodynamics, *Journal of applied physics,* Vol. 27, No. 3, pp. 240–253, 1956.
[21] A. E. Abouelregal, H. Ersoy, Ö. Civalek, Solution of Moore-Gibson-Thompson equation of an unbounded medium with a cylindrical hole, *Mathematics,* Vol. 9, No. 13, pp. 1536, 2021.

Appendix A

Comparison of limiting behavior under GN-III and MGT thermoelasticity:

The choice of heat conduction model significantly influences the limiting behavior of wave propagation in thermoelastic media. In this section, we compare the asymptotic characteristics of Love-type wave fronts under the Green–Naghdi type III (GN-III) and Moore–Gibson–Thompson (MGT) frameworks, focusing on low- and high-frequency regimes.

1. *Low-Frequency Limit* ($w \to 0$)

Table A.1:Asymptotic behavior of wave fronts in the low-frequency limit

Feature	GN-III Model	MGT Model
Thermal wave speed	finite, non-dissipative	finite, dissipative
Second front behavior	persists with weak dispersion	disappears entirely
Phase velocity of 1st front	$c_{L_1} \to c_t^{(2)}$	same
Phase velocity of 2nd front	$c_{L_2} \to c_j^{(i)} \neq 0$	$c_{L_2} \to 0$
Attenuation	Negligible	vanishes for 1st front; 2nd front ceases to propagate

Under GN-III, the second front remains active at low frequencies due to nonlocal conduction, though its influence is minimal. In contrast, the MGT model predicts complete suppression of the second front as $w \to 0$, reflecting its dependence on thermal relaxation dynamics.

2. *High-Frequency Limit* ($w \to \infty$)

Table A.2: Dispersive amplification and thermal dominance at high frequencies

Feature	**GN-III Model**	**MGT Model**
Thermal wave speed	finite, non-dissipative	finite, causal, and dispersive
Phase velocity of 1st front	$c_{L_1} \to c_t^{(1)}$	same
Phase velocity of 2nd front	saturates or oscillates	$c_{L_2} \to \infty$
Attenuation	mild frequency dependence	strong frequency dependence
Energy ratio E	slowly varying	peaks and fluctuates with frequency

At high frequencies, GN-III predicts bounded wave speeds and mild dispersion. The MGT model, however, introduces strong attenuation and unbounded phase velocity for the second front, consistent with causal thermal wave propagation and third-order temporal dynamics.

Appendix B

Visual distinction between causal and non-dissipative thermoelastic wave models:

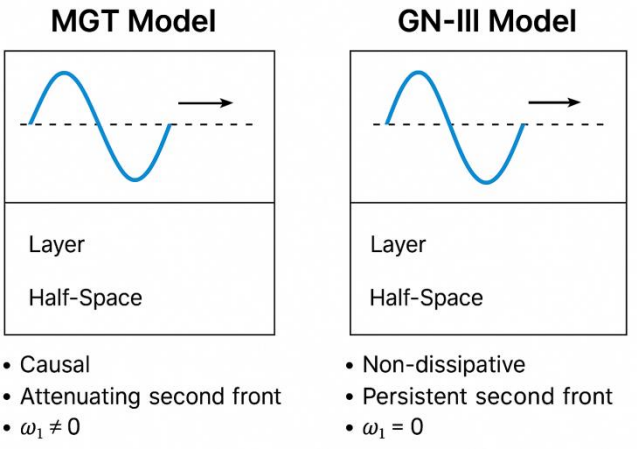


Figure B.2: Dispersive amplification and thermal dominance at high frequencies

The graphical abstract visually contrasts the behavior of Love-type surface waves in double-porosity thermoelastic media under Moore–Gibson–Thompson (MGT) theory and Green–Naghdi type III (GN-III) theory. On the left, the MGT-based model depicts a layered medium with dual porosity, where the first wave front remains non-attenuating, while the second front emerges as dispersive and attenuating due to thermal relaxation effects. This configuration is characterized by key features, including causal conduction, thermal memory, and the presence of a nonzero attenuation coefficient. On the right, the GN-III model shares the same geometry but exhibits persistent, non-dissipative wave fronts. The second front remains active across all frequencies, with labels indicating nonlocal conduction and the absence of attenuation $w_1 = 0$. This visual comparison underscores the enhanced physical realism introduced by MGT theory, particularly its ability to model frequency-sensitive attenuation and the disappearance of the second front in the low-frequency regime—phenomena not captured by GN-III.

Appendix C

The coefficients are defined in terms of coupling parameters and modal amplitudes as:

- *Tier I: Primary coupling matrix*

$$Z_1 = S_1^{(1)} S_2^{(1)} (\Omega_{2c_1}^{(2)} - \Omega_{2c_2}^{(2)})(G_2^{(1)} H_1^{(1)} - G_1^{(1)} H_2^{(1)}),\ Z_2 = S_1^{(2)} S_2^{(2)} (\Omega_{2c_2}^{(1)} - \Omega_{2c_1}^{(1)})(G_1^{(2)} H_2^{(2)} - G_2^{(2)} H_1^{(2)}),$$
$$Z_3 = S_1^{(1)}[S_1^{(2)} (\Omega_{2c_2}^{(1)} - \Omega_{2c_2}^{(2)})(G_1^{(1)} H_1^{(2)} - G_1^{(2)} H_1^{(1)}) \quad Z_4 = S_2^{(1)}[S_1^{(2)} (\Omega_{2c_1}^{(1)} - \Omega_{2c_2}^{(2)})(G_1^{(2)} H_2^{(1)} - G_2^{(1)} H_1^{(2)})$$
$$+ S_2^{(2)} (\Omega_{2c_1}^{(2)} - \Omega_{2c_2}^{(1)})(G_1^{(1)} H_2^{(2)} - G_2^{(2)} H_1^{(1)})], \qquad + S_2^{(2)} (\Omega_{2c_1}^{(1)} - \Omega_{2c_1}^{(2)})(G_2^{(1)} H_2^{(2)} - G_2^{(2)} H_2^{(1)})].$$

- *Tier II: Parametric frequency matrix*

$$Z_1' = S_1^{(1)} K^{(1)} (S_2^{(1)} \alpha^{(1)} (\Omega_{3c_1}^{(2)} - \Omega_{3c_2}^{(2)})(\Omega_{3c_1}^{(1)} - \Omega_{3c_2}^{(1)})_1 + S_1^{(2)} \alpha^{(2)} \Omega_{3c_1}^{(1)} (\Omega_{3c_2}^{(2)} - \Omega_{3c_2}^{(1)})],$$

$$Z_2' = S_1^{(2)} S_2^{(2)} K^{(2)} \alpha^{(2)} (\Omega_{3c_1}^{(1)} - \Omega_{3c_2}^{(1)})(\Omega_{3c_1}^{(2)} - \Omega_{3c_2}^{(2)}),$$

$$Z_3' = S_1^{(1)}[S_2^{(2)} (\Omega_{3c_1}^{(2)} - \Omega_{3c_2}^{(1)})(K^{(1)} \alpha^{(2)} \Omega_{3c_1}^{(1)} - K^{(2)} \alpha^{(1)} \Omega_{3c_2}^{(2)})$$
$$- S_1^{(2)} K^{(2)} \alpha^{(1)} \Omega_{3c_1}^{(2)} \times (\Omega_{3c_2}^{(1)} - \Omega_{3c_2}^{(2)}),$$

$$Z_4' = S_2^{(1)}[S_1^{(2)} (\Omega_{3c_1}^{(1)} - \Omega_{3c_2}^{(2)}) K^{(2)} \alpha^{(1)} \Omega_{3c_1}^{(2)} - K^{(1)} \alpha^{(2)} \Omega_{3c_2}^{(1)})$$
$$+ S_2^{(2)} \times (\Omega_{3c_1}^{(1)} - \Omega_{3c_1}^{(2)})(K^{(1)} \alpha^{(2)} \Omega_{3c_2}^{(1)} - K^{(2)} \alpha^{(1)} \Omega_{3c_2}^{(2)}]$$

- *Tier III: Composite nonlinear matrix*

$$Z_1'' = (S_1^{(1)})^2 S_1^{(2)} \Omega_{3c_2}^{(1)} (\Omega_{3c_2}^{(1)} - \Omega_{3c_2}^{(2)})(K^{(1)} \alpha^{(2)} \Omega_{3c_2}^{(1)} - K^{(2)} \alpha^{(1)} \Omega_{3c_1}^{(2)})$$
$$+ (S_2^{(1)})^2 S_1^{(2)} \Omega_{3c_1}^{(1)} (\Omega_{3c_1}^{(1)} - \Omega_{3c_2}^{(2)})(K^{(1)} \alpha^{(2)} \Omega_{3c_2}^{(1)} - K^{(2)} \alpha^{(1)} \Omega_{3c_1}^{(2)})$$
$$+ (S_1^{(1)})^2 S_2^{(2)} \Omega_{3c_2}^{(1)} (\Omega_{3c_2}^{(1)} - \Omega_{3c_1}^{(2)})(K^{(2)} \alpha^{(1)} \Omega_{3c_2}^{(2)} - K^{(1)} \alpha^{(2)} \Omega_{3c_1}^{(1)})$$
$$+ (S_2^{(1)})^2 S_2^{(2)} \Omega_{3c_1}^{(1)} (\Omega_{3c_1}^{(1)} - \Omega_{3c_1}^{(2)})(K^{(2)} \alpha^{(1)} \Omega_{3c_2}^{(2)} - K^{(1)} \alpha^{(2)} \Omega_{3c_2}^{(1)})$$

$$Z_2'' = S_1^{(1)} S_2^{(1)}[S_1^{(2)} K^{(1)} \alpha^{(2)} \{(\Omega_{3c_2}^{(1)})^2 (\Omega_{3c_2}^{(2)} - \Omega_{3c_1}^{(1)}) + (\Omega_{3c_1}^{(1)})^2 (\Omega_{3c_2}^{(2)} - \Omega_{3c_2}^{(1)})\}$$
$$+ S_2^{(2)} K^{(1)} \alpha^{(2)} \{(\Omega_{3c_1}^{(1)})^2 (\Omega_{3c_2}^{(1)} - \Omega_{3c_1}^{(2)}) + (\Omega_{3c_2}^{(1)})^2 (\Omega_{3c_1}^{(1)} - \Omega_{3c_2}^{(2)})\}$$
$$+ S_2^{(2)} K^{(2)} \alpha^{(1)} \Omega_{3c_2}^{(2)} \times \{\Omega_{3c_1}^{(1)} (\Omega_{3c_1}^{(2)} - \Omega_{3c_2}^{(1)}) \Omega_{3c_1}^{(2)} \Omega_{3c_2}^{(1)})\}$$
$$+ S_1^{(2)} K^{(2)} \alpha^{(1)} \Omega_{3c_1}^{(2)} \{\Omega_{3c_1}^{(1)} (2\Omega_{3c_2}^{(1)} - \Omega_{3c_2}^{(2)}) - \Omega_{3c_2}^{(1)}) \Omega_{3c_2}^{(1)} \Omega_{3c_2}^{(2)}\}],$$

$$Z_3'' = S_2^{(1)} (\Omega_{3c_2}^{(1)} - \Omega_{3c_1}^{(1)})(\Omega_{3c_1}^{(2)} - \Omega_{3c_2}^{(2)})$$
$$\times \{(S_1^{(1)})^2 K^{(1)} \alpha^{(1)} \Omega_{3c_2}^{(1)} - S_1^{(2)} S_2^{(2)} K^{(2)} \alpha^{(2)} \Omega_{3c_1}^{(1)}\},$$

$$Z_4'' = S_1^{(1)} (\Omega_{3c_2}^{(1)} - \Omega_{3c_1}^{(1)})(\Omega_{3c_2}^{(2)} - \Omega_{3c_1}^{(2)})$$
$$\times \{(S_1^{(1)})^2 K^{(1)} \alpha^{(1)} \Omega_{3c_1}^{(1)} - S_1^{(2)} S_2^{(2)} K^{(2)} \alpha^{(2)} \Omega_{3c_2}^{(1)}\}.$$

For indices $i, j = 1, 2$, define:

$$\Omega_{3c_j}^{(i)} = \frac{\alpha^i w^2 - (c_j^{(i)})^2 \eta_1^{(i)}}{\gamma_1^{(i)} (c_j^{(i)})^2}$$

and symmetric and antisymmetric modal combinations

$$P = S_1^{(1)} + S_2^{(1)},\ Q = S_1^{(1)} - S_2^{(1)}.$$

Notation

Symbol	Description	SI Unit
$X = (x_1, x_2, x_3)$	spatial coordinate vector	m
t	time variable	s

$u=(0,u_2,0)$	displacement vector (assumed 2D motion)	m
T_0	reference state temperature	K
$T-T_0$	temperature increment from the reference state	K
φ,ψ	void volume fraction (first and second kind)	dimensionless
a	thermal heat capacity per unit volume	J·m^{-3}·K^{-1}
λ,μ	Lamé's elastic constants	Pa (N·m^{-2})
ρ	mass density of the material	kg·m^{-3}
χ_1,χ_2	equilibrated inertia (first and second kinds of voids)	kg·m^{-3}
β	thermoelastic coupling coefficient	Pa·K^{-1}
b,d	elasto-voids coupling coefficients	dimensionless
b_1	contaminant-related material constant	dimensionless
$\alpha,\alpha_1,\alpha_2,\alpha_3$	material constants due to pore contaminants	dimensionless
γ_1,γ_2	thermal constitutive coefficients	Pa·K^{-1}
t_{ij}	stress tensor components	Pa
$2\varepsilon_{ij}=u_{i,j}+u_{j,i}$	strain tensor components	dimensionless
$\bar{Q}=(\bar{Q}_1,\bar{Q}_2,\bar{Q}_3)$	heat flux vector	W·m^{-2}
ξ,ζ	intrinsic equilibrated body force (first and second kind)	N·m^{-3}
λ_2^c,λ_3^c	coupling parameters	Pa
∇, ∇^2	Gradient and Laplacian operator	m^{-1}, m^{-2}
τ_0,τ_1	second- and first-order thermal relaxation times	s
$\beta=(3\lambda+2\mu)\alpha_t$	thermoelastic coupling coefficient	Pa·K^{-1}
α_t	coefficient of thermal expansion	K^{-1}
k , k^*	Thermal and non-classical conductivity coefficient	W·m^{-1}·K^{-1}
ϑ	thermal displacement field	m
η	unifying parameter (e.g., damping, coupling)	dimensionless
γ	general material constant	dimensionless